UNIVERSITY OF HELSINKI REPORT SERIES IN PHYSICS

HU-P-D176

The Path to a Porous Semiconductor Multilayer

Ari Harjunmaa

Division of Materials Physics
Department of Physics
Faculty of Science
University of Helsinki
Helsinki, Finland

ACADEMIC DISSERTATION

To be presented, with the permission of the Faculty of Science of the University of Helsinki, for public criticism in the Auditorium A129 of the Department of Chemistry (Chemicum), on February 11th, 2011, at 12 o'clock p.m.

HELSINKI 2011

ISBN 978-952-10-5989-6 (printed version)
ISSN 0356-0961
Helsinki 2011
Helsinki University Printing House (Yliopistopaino)

ISBN 978-952-10-5990-2 (PDF version)
http://ethesis.helsinki.fi/
Helsinki 2011
Electronic Publications @ University of Helsinki (Helsingin yliopiston verkkojulkaisut)

Ari Harjunmaa **The Path to a Porous Semiconductor Multilayer**, University of Helsinki, 2011, 60 p.+appendices, University of Helsinki Report Series in Physics, HU-P-D176, ISSN 0356-0961, ISBN 978-952-10-5989-6 (printed version), ISBN 978-952-10-5990-2 (PDF version)

Classification (INSPEC): A6146, A6855, A8116
Keywords (INSPEC): porous silicon, cluster, cluster deposition, thin films, multilayer, molecular dynamics

ABSTRACT

Thin films are the basis of much of recent technological advance, ranging from coatings with mechanical or optical benefits to platforms for nanoscale electronics. In the latter, semiconductors have been the norm ever since silicon became the main construction material for a multitude of electronical components. The array of characteristics of silicon-based systems can be widened by manipulating the structure of the thin films at the nanoscale — for instance, by making them porous. The different characteristics of different films can then to some extent be combined by simple superposition.

Thin films can be manufactured using many different methods. One emerging field is cluster beam deposition, where aggregates of hundreds or thousands of atoms are deposited one by one to form a layer, the characteristics of which depend on the parameters of deposition. One critical parameter is deposition energy, which dictates how porous, if at all, the layer becomes. Other parameters, such as sputtering rate and aggregation conditions, have an effect on the size and consistency of the individual clusters.

Understanding nanoscale processes, which cannot be observed experimentally, is fundamental to optimizing experimental techniques and inventing new possibilities for advances at this scale. Atomistic computer simulations offer a window to the world of nanometers and nanoseconds in a way unparalleled by the most accurate of microscopes. Transmission electron microscope image simulations can then bridge this gap by providing a tangible link between the simulated and the experimental.

In this thesis, the entire process of cluster beam deposition is explored using molecular dynamics and image simulations. The process begins with the formation of the clusters, which is investigated for Si_xGe_{1-x} in an Ar atmosphere. The structure of the clusters is optimized to bring it as close to the experimental ideal as possible. Then, clusters are deposited, one by one, onto a substrate, until a sufficiently thick layer has been produced. Finally, the concept is expanded by further deposition with different parameters, resulting in multiple superimposed layers of different porosities.

This work demonstrates how the aggregation of clusters is not entirely understood within the scope of the approximations used in the simulations; yet, it is also shown how the continued deposition of clusters with a varying deposition energy can lead to a novel kind of nanostructured thin film: a multielemental porous multilayer. According to theory, these new structures have characteristics that can be tailored for a variety of applications, with precision heretofore unseen in conventional multilayer manufacture.

Contents

1 INTRODUCTION

An abundant material with a multitude of uses, silicon has benefited mankind with advances in fields varying from electronics to cosmetic surgery. In the former, smaller is better: ever since the advent of the first silicon transistor in 1954 [1], technological improvements have seen the constant decrease of transistor size, a phenomenon widely known as Moore's law [2]. Decreasing volume requirements have led to investigations into other, more expensive materials, widening the array of characteristics at the disposal of electronics manufacturers. For instance, compound semiconductors have not only made possible the now ubiquitous light-emitting diodes, but they have also taken the lead in solar cell efficiency [3; 4; 5].

However, this does not mean that silicon is a thing of the past. In 1990, Leigh Canham discovered that infusing bulk silicon with pores resulted in an upward shift of the photoluminescence wavelength, enough to bring it to the visible range at room temperature [6]. This effect was attributed to quantum confinement within the wirelike nanostructures that had become isolated by the pores [7; 8]. The same effect can be seen in isolated nanocrystals as well as similar systems of other materials, such as germanium or even compound Si/Ge [9; 10]. This discovery gave further motivation to silicon research, as it could now be used for many of the same purposes as compound semiconductors (*e.g.* [11]), but without the risks of increased toxicity or expense.

On an industrial scale, porous silicon manufacture often follows the same principles as Canham's original process, that of anodization. A top-down method, anodization consists of applying a current through a silicon wafer anode immersed in hydrogen fluoride, which corrodes the wafer and makes it porous. Another commonly used method is stain etching, wherein silicon wafers are immersed in solutions of nitric acid, sodium nitrite or nitrogen dioxide in hydrofluoric acid, which causes a corroding surface reaction even without the use of a current [12]. The popularity of these methods stems from the ease of manufacture on a macroscopic scale, as well as from the availability of the required materials.

From a research viewpoint, bottom-up methods may give rise to a much greater range of possibilities, albeit these methods have not yet been perfected for mass production. A method of film growth called ionized cluster beam (ICB) deposition was already known and used prior to Canham's discovery [13]; but the promise of porous materials prompted researchers to reconsider a similar technique, only without acceleration [14; 15; 16]. This so-called low-energy cluster beam deposition (LECBD) of neutral clusters was soon used to construct porous silicon films which were found to exhibit the same photoluminescent characteristics as films obtained through

anodization [17; 18]. In contrast to anodization, the use of cluster beams makes it possible to construct *e.g.* single layers comprising separate nanocrystals of different elements. However, no experimental research in this direction has yet been performed due to the requirement of simultaneous deposition from two or more separate cluster sources. Another unique possibility is multiple superimposed layers (multilayers) of alternating elements and porosities, which would be experimentally feasible with conventional cluster deposition setups but has not yet been attempted.

Free from the material constraints of experimental endeavor, computational physics allows a glimpse into this unexplored line of research. An atomistic simulation technique called molecular dynamics (MD) has been used to model many aspects of experimental cluster deposition, including amorphous and epitaxial film growth [19] as well as porous film growth [20], with results that are satisfactory in complementing experimental findings. It is thus a logical step forward to use this method to extend beyond the reach of current experimental facilities, to foretell the possibilities of more complex cluster-deposited nanostructures.

This thesis work does exactly that: it entails, from beginning to end, the entire cluster deposition process of multielemental multilayers as seen through MD simulations. The beginning takes place at the cluster source, where individual atoms are sputtered from a magnetron source into a gas condensation chamber where the clusters initially take form; within the time it takes for them to be deposited, the clusters settle into energetically favorable structures that may differ from their original morphologies; and finally, the path of the clusters ends at the substrate onto which single layers are grown, one by one, until the desired multilayer construction is achieved.

Over the course of the last few decades, MD simulations have displayed the capability of reproducing, and even predicting, experimental results. The work presented in this thesis is another example of scientifically relevant research that was more practical to first perform using computational methods. Once the possibilities of the novel materials here presented are fully comprehended, it will be worthwhile to take the necessary extra steps to realize them experimentally.

2 PURPOSE AND STRUCTURE OF THIS STUDY

The purpose of this thesis is to provide a detailed overview of the step-by-step process of ionized cluster beam deposition of porous semiconductor multilayers — from cluster formation to the deposited end result — as seen through molecular dynamics simulations. The thesis aims to present a theoretical background to support the concept of a bielemental cluster in thermal equilibrium, and to speculate on its usefulness as a building block for a novel kind of thin film structure with a variety of uses.

This thesis contains, in addition to the summary here introduced, four peer-reviewed publications, presented with the permission of their publishers at the end of this work. These publications provide a basis for the summary, and as such, they are referred to within the text with bold-face Roman numerals.

This summary is structured as follows: in Section 3, an explanation is given as to why bulk characteristics do not accurately describe effects at the nanoscale, and several systems at this size scale are shown as examples of physical incarnations of this behavior. In Section 4, the simulation methods used to study these kinds of systems are introduced. In Section 5, methods for the numerical characterization of simulated clusters and cluster-deposited layers are presented. In Section 6, the results obtained from the simulations are recounted as presented in the publications and further elaborated. Finally, in Section 7, the main points of the thesis and its relevant results are recapitulated.

2.1 Summaries of the original publications

Publication I: Molecular dynamics simulations of Si/Ge cluster condensation, A. Harjunmaa and K. Nordlund, *Computational Materials Science* **47**, 456–459 (2009).

> The formation of Si_xGe_{1-x} clusters (with $x = 0.0, 0.1, \ldots, 1.0$) in an Ar atmosphere is investigated using classical molecular dynamics simulations. The sphericity of the clusters is determined and found to depend directly on x. It is also found that Ge atoms have a tendency to segregate to the surface of the clusters, but that this effect depends on the potential used for the simulations. The clusters are deemed to consist of nanocrystalline regions that are not perfectly aligned to form a single crystal.

Publication II: Structure of Si/Ge nanoclusters: kinetics and thermodynamics, A. Harjunmaa, K. Nordlund, and A. Stukowski, *Computational Materials Science,* In Press, Corrected Proof, Available online 31 December 2010, doi:10.1016/j.commatsci.2010.12.007.

A number of the least ideal clusters (one for each value of x) from the previous study are revisited in an effort to bring them closer to the assumed perfect form. Sphericity and crystallinity are sought to improve with annealing at 1800 K, 3000 K, and 6000 K; elemental segregation is enhanced with the use of a novel Monte Carlo simulation method working in the semi-grand-canonical regime. The results show that the annealing effects depend on the temperature, with only the 6000 K runs clearly improving both sphericity and crystallinity and decreasing the clusters' free energy close to the level of perfect model clusters. With the Monte Carlo simulations, it is demonstrated that the preferred location of Ge atoms in a cluster is at the surface.

Publication III: MD simulations of the cluster beam deposition of porous Ge, A. Harjunmaa, J. Tarus, K. Nordlund, and J. Keinonen, *The European Physical Journal D* **43**, 165–168 (2007).

Using thermalized spherical clusters cut out from crystalline bulk, the low-energy cluster beam deposition of Ge clusters on a Si surface is simulated with molecular dynamics. The porosity of the resulting layers is investigated as a function of deposition energy, and it is shown that the transition from porous to non-porous happens between energies of about 10 meV/atom and 1 eV/atom. In addition, transmission electron microscope image simulations of the layers are performed, and a comparison of the images of layers of differing porosities is presented.

Publication IV: Growing multiple layers of porous semiconductors — A molecular-dynamics study, A. Harjunmaa and K. Nordlund, *EPL* **91**, 26002 (2010).

The deposition is continued atop the porous layers obtained in the previous study. This time, the objective is to grow multiple layers of alternating porosities. The critical issue of how well a porous layer can withstand the high-energy deposition of more clusters on top is investigated, and density profiles for the new multilayers are presented, thus proving that the original porous layers remain intact after the additional deposition. Furthermore, transmission electron microscope images of the layers are provided and the contrast of different elements is investigated.

2.2 Author's contribution

The author designed, set up, and carried out all of the simulations and analysis of the results in all publications, except for the thermalization of the Ge cluster in publication **III**, which had been done by Jura Tarus prior to the beginning of the study. The SGCMC addition to the Lammps code used in publication **II** was implemented by Alexander Stukowski.

The author wrote all publications in their entirety.

3 NANOSCALE SEMICONDUCTORS

The ongoing fulfillment of Moore's law has led technology into a new millenium where transistor size is measured in nanometers. While, at one time, "there [was] plenty of room at the bottom" [21], a limit not anticipated by physicists in the 1960s has already been reached: the size of the atom. While it certainly is impossible to build components smaller than their constituent parts, material characteristics start to change already when merely approaching this size scale from above. Fortunately, this effect can give rise to new possibilities instead of just barring the way of the old ones, thus creating the new field of *nanotechnology*.

3.1 Deviation from bulk characteristics

Different materials have a variety of characteristics which make them suitable for use for different purposes. These characteristics, such as melting or boiling point, thermal or electric conductivity, photoluminescence wavelength, etc., have been tabulated into extensive databases containing information for not only single elements, but complex molecules and composites as well. This information has been empirically determined for tangible amounts of the materials in question. As such, they are referred to as *bulk values*.

When the amount of material decreases, some of these values change. The material can no longer be treated as a continuum of atoms, each of which contributes similarly to the bulk. If there are few enough atoms in a system, the contribution of a single atom has a proportionally larger impact on the whole — much like when removing singers from a choir, all the way down to a quartet, where the voice of an individual singer can be distinguished.

3.1.1 Surface energy

When considering a perfectly crystalline bulk material, its surface is the only place where atoms behave differently. This is because their number of nearest neighbors is reduced, thus altering the energetics of the local environment when compared to within the bulk. To create a surface, *e.g.* by slicing a bulk lattice in two, energy is needed; this *surface energy* is stored in the surface atoms. In the macroscopic world, the effect of this difference in atomic energies is drowned by the overwhelming majority of bulk atoms.

At the nanoscale, the effect becomes noticeable. Consider a sphere of radius r and volume $V = 4\pi r^3/3$ with a homogeneous density of atoms. The surface atoms cover the area $A = 4\pi r^2$

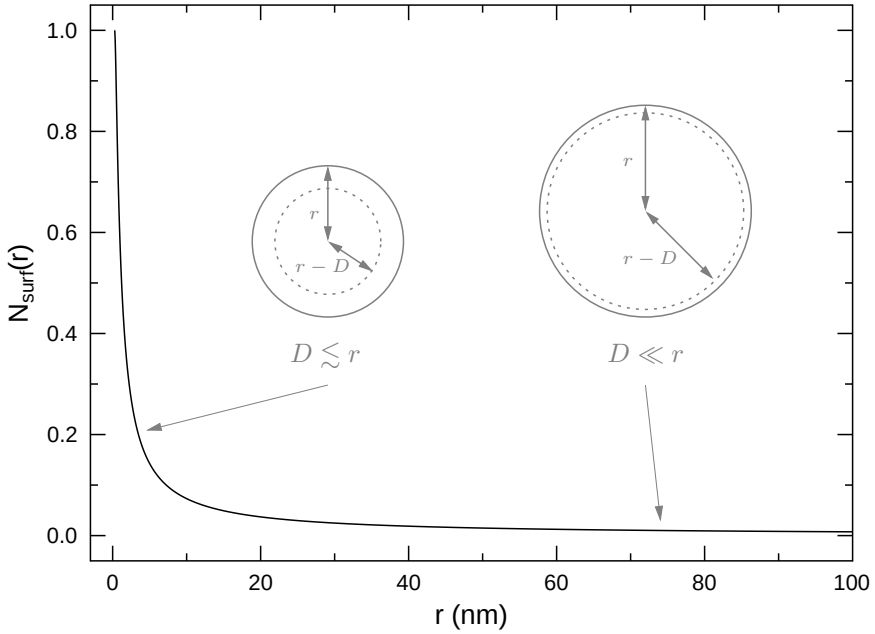

Figure 1: The ratio of surface atoms to the total number of atoms in a sphere as a function of sphere radius, or Eq. 1. The parameter D is set to 0.25 nm, approximating the thickness of a single atomic layer.

down to a depth of D, or a volume of $V_{surf} = 4\pi(r^3 - (r-D)^3)/3$. That means that the portion of surface atoms in the sphere is

$$N_{surf}(r) = 1 - \frac{(r-D)^3}{r^3}. \tag{1}$$

From the plot of this function shown in Fig. 1, it is clear that as the diameter of the sphere drops below about 10 nm (or $40D$), the role of surface atoms becomes drastically more important.

One of the most obvious examples of this effect is its impact on the melting or boiling points of a material. Even before the advent of nanotechnology, it was experimentally discovered that the melting point of nanoscale gold particles depends on the size of the particle [22]. When a material melts, it loses the rigidity of the angular distribution of its atoms, which gain more freedom of movement about each other. When a material boils, this freedom is extended not only to the angular distribution, but to the interatomic distances as well. A certain amount of thermal energy is needed to reach melting and boiling; if a material already has a higher-than-bulk portion of surface energy, it will need less additional thermal energy to reach its melting or boiling point. Thus, as the size of a system of atoms drops below about 10 nm, its melting and boiling points will consequently drop.

3.1.2 Quantum confinement

Extending the work of Max Planck and Albert Einstein in his PhD thesis of 1924, Louis de Broglie postulated that all matter had characteristic features of both waves and particles [23]. This *wave-particle duality* implied that *e.g.* electrons, formerly thought of merely as negatively charged point-like particles orbiting a positively charged nucleus, could also be mathematically depicted as photon-like wave packets using a *wave function* $\psi(\mathbf{r}, t)$, which describes the probability of finding the electron at the location $\mathbf{r}$ at time t through $P(\mathbf{r}, t) = |\psi(\mathbf{r}, t)|^2$. These wave functions are solutions that satisfy the Schrödinger equation

$$i\hbar\frac{\partial}{\partial t}\psi(\mathbf{r}, t) = -\frac{\hbar^2}{2m}\nabla^2\psi(\mathbf{r}, t), \tag{2}$$

where $\hbar = h/2\pi$ is the normalized Planck's constant and m the mass of the electron. For a free electron, the wave function can be presented in the simple form

$$\psi(\mathbf{r}, t) = Ae^{i(\mathbf{k}\cdot\mathbf{r}-\omega t)}, \tag{3}$$

where $\mathbf{k}$ is the wavevector, ω is the angular frequency, and A is a constant. Inserting this into Eq. 2, we find that

$$\hbar\omega = \frac{\hbar^2 k^2}{2m} \equiv E, \tag{4}$$

also known as the *dispersion relation* that defines the electron's energy E [24].

In metals, electrons can be considered to be free particles; in semiconductors and insulators, however, they cannot. Instead, they are confined to *orbitals* around potential wells formed by atomic nuclei in what is called the *tight-binding approximation*. Each orbital corresponds to an energy level, the lowest of which in a one-atom system can be denoted as E_0. The addition of an atomic lattice around this single atom influences this energy level, which then becomes

$$E(k) = E_0 + 2I_0\cos(ka), \tag{5}$$

where a is the periodic interatomic distance in one lattice direction (or *lattice constant*) and I_0 a value that describes the strength of the influence, *i.e.* the ease of electronic transfer from one atom's ground level energy to its neighbor's [25]. Thus, instead of the discrete energy levels E_n ($n = 0, 1, 2, \ldots$) of single atoms, continuous *energy bands* of size $4I_n$ are formed around E_n. The level around E_0 is referred to as the *valence band* and the level around E_1 is referred to as the *conduction band*, since only electrons in the latter can contribute to electrical conduction.

There is an *energy gap* E_g between the two bands that electrons can cross with the help of excess energy provided by anything from an electric field to photon irradiation. If the amount of required energy is easily obtained, the material is classified as a semiconductor; if not, it is an insulator.

Strictly speaking, Eqs. 4 and 5 are not continuous functions of k; rather, they are divided into discrete energy levels due to quantum constraints on the wavevector. These constraints stem from the periodicity of the crystalline lattice, since k is inversely proportional to the wavelengths of lattice vibrations, which in turn are confined to the exact interatomic distances of a periodic lattice. When the size scale is reduced and the system contains a numerable N atoms in one dimension, Eq. 5 becomes

$$E(m, N) = E_n + 2I_n \cos\left(\frac{m\pi}{N+1}\right) = E_n + 2I_n \cos(k_m a), \tag{6}$$

where m is an integer *quantum number* between 1 and N, and

$$k_m = \frac{m\pi}{(N+1)a}. \tag{7}$$

The connection to bulk can be seen as $N \to \infty$, when k becomes continuous between 0 and π/a (a region known as the *Brillouin zone*) and $E(k)$ becomes continuous along the whole valence band [26]. However, when $N \to 0$, the discretization of the energy levels becomes obvious as the possible values of k_m decrease. Because m cannot equal either 0 or $N + 1$, the highest energy value below the gap and the lowest value above it eventually diverge from the bulk values, stretching E_g. This effect is depicted in Fig. 2.

The widening of the energy gap in nanoscale semiconductor systems is noticeable through phenomena that depend on the energy gap, such as photoluminescence, in which a material absorbs photons, the energy of which *excites* electrons, helping them cross the energy gap. When excited electrons relax back over the gap, a photon with an energy of E_g is emitted. With a widened energy gap, the wavelength of the emitted light is consequently shifted downward from the bulk value. This explains why porous silicon, which can be considered as an array of consecutive pillars of silicon of small enough breadth to contain a numerable amount of atoms, exhibits a shift in photoluminescence wavelength.

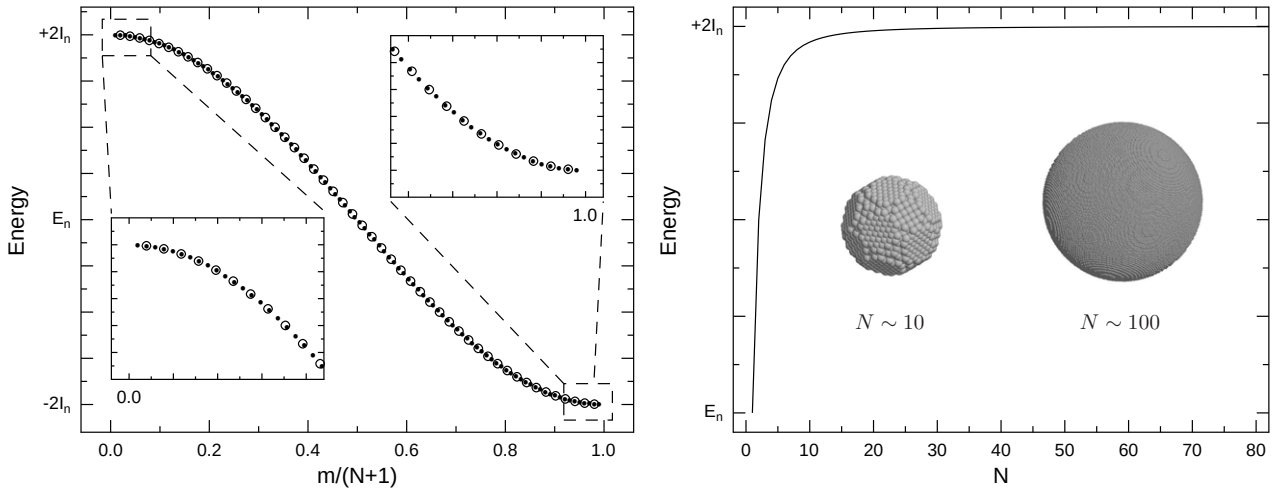

Figure 2: Left: as the N of Eq. 6 is decreased from 100 (dots) to 50 (empty circles), the energy values closest to the band edges diverge from $E_n \pm 2I_n$ as clarified in the insets. Right: the highest band edge energy is shown as a function of N.

3.2 Nanoclusters and their applications

The above-mentioned effects are realized in *nanostructures*, which are systems of atoms where at least one dimension is confined to less than about 100 nm. Examples of a singly confined dimension orthogonal to two macroscopic ones are nanostructured surfaces such as nanometer-thin films; two nanometric dimensions mean that the structure is a *nanowire* or a *nanotube*; and if all dimensions are on the nanoscale, we speak of *nanoparticles* or *nanoclusters*. The latter correspond best to the systems described above in that they are spherical or near-spherical collections of atoms with a small radius, implying a small number N of atoms in every dimension.

Nanoparticles are not merely the product of technological advance; they exist in nature as well. The nucleation of aerosol particles is a widely researched topic in atmospheric science, since atmospheric clusters are responsible for instigating cloud formation. This shared interest in nanosize particles means that a portion of the methodology of both atmospheric and materials sciences, two fields of very different scope, is actually quite similar. Particle nucleation obeys the same basic principles for aerosol particles in a nitrogen atmosphere as it does for semiconductor particles in a noble gas atmosphere.

Clusters not in chemically or gravitationally induced contact with a bulk substance are called free clusters. On the materials science side, research into free clusters has been extensive [27], since to map the exact impact of cluster size on non-bulk effects, any possible interference from bulk atoms has to be avoided. However, for obvious reasons, the lifetime of free clusters is very

short, and so they have very few practical applications by themselves. Fortunately, many of the clusters' extraordinary characteristics are retained when supported by or embedded into a bulk of a different material. Even support from a bulk of the same element is often sufficient, as is seen in the case of porous films acquired through top-down methods. This gives rise to numerous possibilities in using clusters for electronics applications.

3.2.1 Cluster-assembled thin films

In addition to visible photoluminescence from semiconductor nanoclusters, there are many other interesting effects in systems of this size, such as the transition of silicon clusters from covalent to metallic for clusters of less than about 50 atoms [28]. These kinds of effects are of great interest to electronics manufacturers for applications at an industrial scale. However, the effect of a single cluster with this few atoms is diminutive; to reproduce the desired effect on a macroscopic scale, clusters have to be present in macroscopic amounts. Fortunately, it has been discovered that it is possible to conserve the original structures, and therefore the original characteristics, of these clusters even when depositing them in large amounts [29]. This has given the motivation to develop the ICB and LECBD techniques to grow films using nanoclusters as building blocks.

Different cluster beam techniques can be categorized by the energy used in the deposition. In the ICB technique, the clusters are ionized after formation, which allows them to be accelerated using an electric field. The energy of the clusters is typically of the order of several eV/atom, which is enough to cause some melting and deformation of the clusters upon impact, but which will not destroy the original cluster morphologies completely, as shown in Fig. 3. Increasing the clusters' energies further (up to the MeV/atom range) takes the deposition into the realm of *high-energy cluster beam bombardment*, which has destructive effects on the integrities of both the deposited clusters as well as the bombarded substrate [29].

As the name suggests, LECBD uses low-energy clusters that undergo no separate acceleration after the formation stage — hence, there is no need for separate ionization equipment. These clusters travel at thermal energies (measured in meV/atom) until they encounter the deposition substrate softly enough to avoid any deformation. Naturally, spherical clusters piled on top of each other leave spaces between themselves, reducing the density of the film and making it, in effect, porous. Thus, the same kind of porous film that is most often made using anodization can be achieved with a cluster deposition technique.

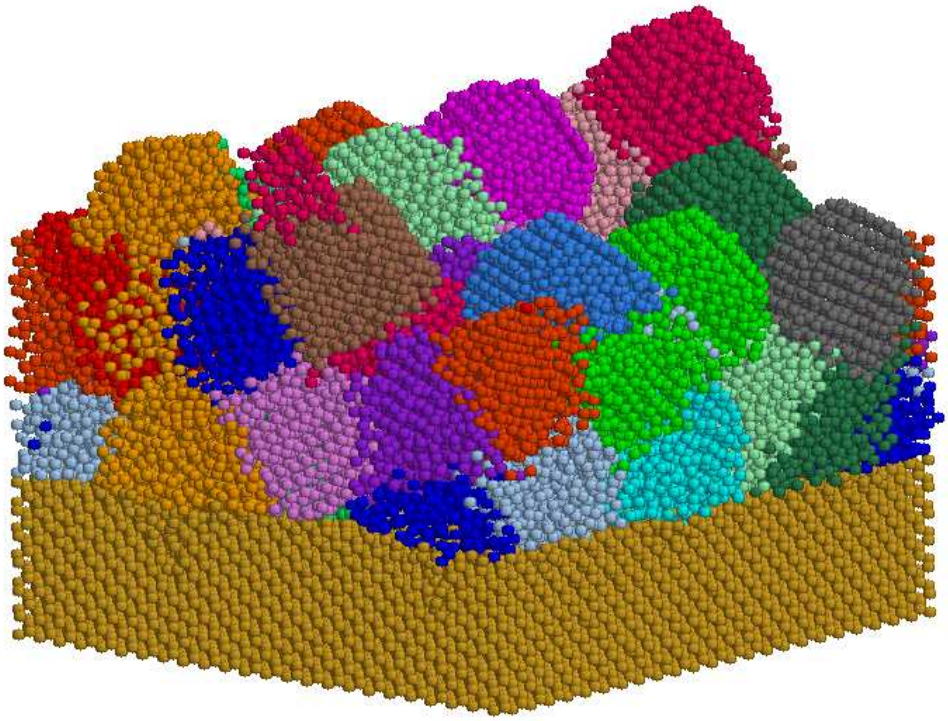

Figure 3: A graphic representation of the simulated deposition of 40 Ge clusters onto a Si substrate at 1 eV/atom, made using the program RasMol [30]. The original clusters of 1018 atoms each are shown in different colors.

While porosity in anodized films can be varied as a function of the anodization charge (current or time), the same effect can be achieved in cluster-deposited films by varying the acceleration voltage. However, the photoluminescence wavelength shift, while clearly a function of anodization charge [6; 31], is not strictly related to the layer porosity. This is because the magnitude of the quantum confinement effect depends purely on the dimensions of the individual nanostructures that make up the porous layer, on which the acceleration voltage, up to a certain point, has no impact. Instead, varying the size of the deposited clusters, while having no direct effect on porosity, has the desired effect on the wavelength shift [32]. Furthermore, the layer need not even be porous as long as the morphology of the original clusters is conserved in the deposition.

3.2.2 Multilayer waveguides

Besides the already mentioned effect on the photoluminescence wavelength, the porosity of a layer also has an effect on its refractive index. In essence, pores are simply voids where the speed of light is at its highest, and so an increase in porosity results in a lowering of the layer's refractive index. Therefore, a layer of low porosity sandwiched between two layers of high

porosity is effectively a waveguide that can carry along light due to total reflection from the layer interfaces.

Porous silicon multilayers can be constructed using anodization by varying the current at intervals corresponding to the desired layer thicknesses [33; 34]. Their usefulness was first demonstrated as Bragg reflectors and Fabry-Perot filters [35], although it did not take long to suggest their use as waveguides [36; 37]. What *has* taken a long time, however, is making the connection between LECBD and porous multilayers; depositing clusters onto a porous layer may intuitively seem to simply fill up the pores. It is the aim of this thesis to show that this is not the case.

4 SIMULATION METHODS

This thesis presents a study that is completely computational in nature. The dynamic development of the investigated systems is modeled using methods that are primarily based on classical molecular dynamics. In addition to this, simulations of transmission electron microscope images are used to view some of the obtained final atomistic configurations. In this section, these computational methods are reviewed and their application to experimental work is expounded.

4.1 Classical molecular dynamics

The molecular dynamics simulation technique was developed by Berni Alder at the end of the 1950s [38; 39; 40]. It has since demonstrated its usefulness in modeling nanoscale systems and predicting their behavior over microscopic time scales. Classical MD still remains amidst the most widely used computational methods in materials research, fueled by ever-improving CPU speeds that make possible the investigation of ever larger systems over ever longer periods of time.

In this study, two different MD programs are used: for publications **I**, **III**, **IV**, and half of the simulations in publication **II**, the program Parcas [41; 42]; and for the other half of the simulations in publication **II**, the program Lammps [43].

4.1.1 The MD algorithm

The MD algorithm is a deterministic method of calculating the evolution of a system over time from its starting configuration. Such a system (or *simulation cell*) consists of a predefined number of atoms, of which three values are known and tracked throughout the simulation: type, location, and velocity. Usually, the type of atom (*i.e.* its element) stays constant, but the location and velocity coordinates $\mathbf{r}$ and $\mathbf{v}$ change as the atoms interact with each other. These interactions are quantified and $\mathbf{r}$ and $\mathbf{v}$ are updated accordingly over small periods of time Δt called *time steps*. Thus, a simulation run comprises a number of consecutive time steps in which these calculations and updates are performed anew.

Since the interactions and coordinates depend on each other, the simulation is at its most accurate at the limit $\Delta t \to 0$. However, the length of the time step must be non-zero for there to be a finite amount of steps for the computer to process — the longer the time step, the faster the simulation. Therefore, Δt must be defined using specific conditions that make

it as large as possible while allowing the simulation to remain realistic. The most important consideration is that the total energy of the system must be conserved; this has the effect of limiting the atomic displacements to a fraction of the average interatomic distance. Naturally, as the system evolves, the conditions may change; this is why it is efficient to employ an adaptive time-step that is constantly regulated to optimize CPU use [44].

Optimization is a key concern in making an efficient MD algorithm. As the size of the system is made larger, the amount of possible atom-to-atom interactions is exponentially increased. When dealing with systems of thousands of atoms or more, calculating all interactions would take an immense amount of time. The amount of required calculations can be drastically reduced by ignoring those where the involved atoms are separated by more than a specified cut-off distance. Furthermore, the atoms in areas thus delimited can be grouped into periodically updated neighbor lists that remove the need to calculate their proximity at each time step.

Any time an approximation is made to optimize calculation efficiency, an amount of information is lost in the process. Sometimes, this loss can even lead to incorrect results if care is not taken to ensure the validity of the approximation when used for a specific purpose. For instance, according to the Born-Oppenheimer approximation [45], which is the basis of classical MD, electrons in a system can reach electronic equilibrium much faster than atomic nuclei, making it possible to treat them independently and ignore any electron-nucleus coupling. This allows the treatment of atoms in MD simulations as single entities that only interact with each other, making the simulations much faster; however, any physical process in which the interactions between electrons and the atomic lattice have a significant role (*e.g.* cooling of metallic systems) can then not be accurately described [46; 47]. This concern has been addressed in first-principles methods (or *ab-initio MD*) based on quantum mechanical models such as density functional theory that take a system's electronic behavior into consideration — accordingly, these methods are much more CPU-intensive and cannot reach the size and time scales of classical MD.

Even with trivial approximations, great care must be taken to ensure that a simulated system appropriately describes the physical world. For example, to simulate bulk matter, the computationally costly problem of the presence of an immense number of atoms is solved with the use of *periodic boundary conditions*. This means that an edge of a simulation cell is treated as a portal to the opposite edge of the cell, so that atoms at one edge interact with atoms at the other edge as if they were neighbors. This allows a very small cell to be the basis of an entire macroscopic bulk. However, there are two important considerations:

- the atomic configurations of the opposite edges must be compatible;

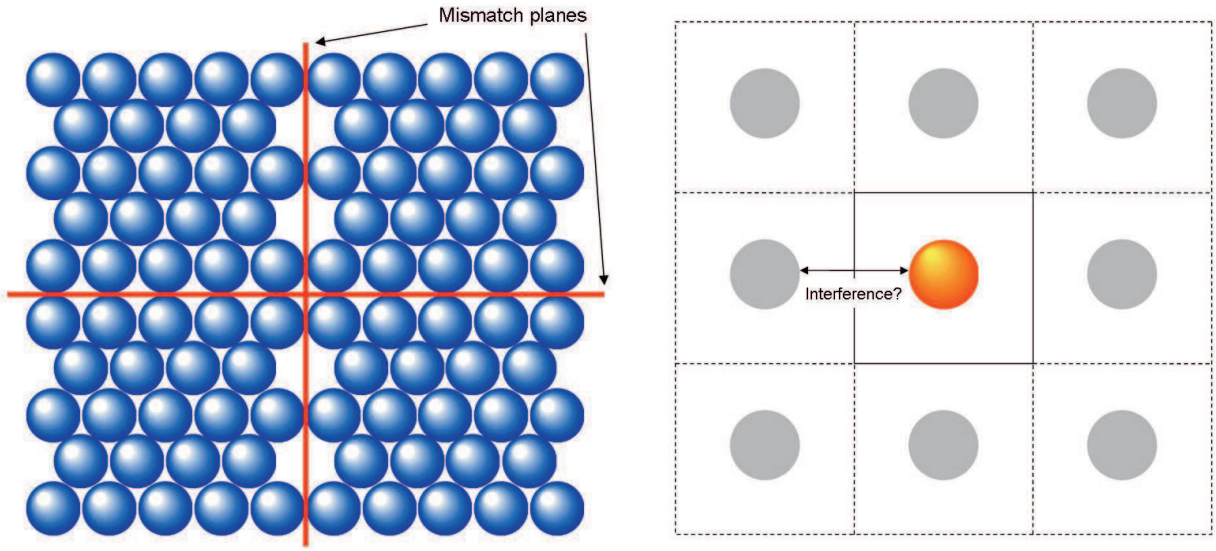

Figure 4: Left: an incorrect duplication of a simulation cell that causes mismatch planes at all edges. Right: a questionably small unit cell may result in unphysical interference between a defect and its virtual image.

- there must be a sufficient border region clean of any influence of possible defects within the cell.

Instances of these considerations are shown in Fig. 4.

If the atomic configurations are not straight continuations of each other, they will cause a *mismatch plane* loaded with potential energy that may disrupt the entire simulation. This is not generally a problem when simulating level crystalline lattices, but a tilt in the lattice makes the possibility of a mismatch much more likely. And if the simulation cell is too small, the influence of a defect may reach over the edge and affect itself from the other side.

4.1.2 Interatomic potentials

The above-mentioned atomic interactions are depicted by so-called *interatomic potentials*. These are empirical or semi-empirical sets of parameters for mathematical models used to calculate the interactions between two or more atoms, based on relative geometric considerations (*i.e.* distance and angle). The general form for a potential function Φ describing interactions

between N particles (with indices $i, j, k, \ldots$) is

$$\Phi(1,\ldots,N) = \sum_i f_1(i) + \sum_{i<j} f_2(i,j) + \sum_{i<j<k} f_3(i,j,k) + \ldots + f_N(1,\ldots,N), \tag{8}$$

where f_n is an n-body function characteristic to a specific potential (except for f_1, which normally describes external forces similarly exerted on each particle). As n increases, the required computation time to calculate f_n rises exponentially; normally, f_n is made to converge to zero for $n > 3$.

The simplest example for a two-body case is a *pair potential*, a single function $f_2(r_{ij})$ where r_{ij} is the distance between two atoms i and j, such as the Lennard-Jones potential, which is often used to describe the behavior of noble gases [48; 49]:

$$f_2(r_{ij}) = 4\varepsilon \left[\left(\frac{\sigma}{r_{ij}} \right)^{12} - \left(\frac{\sigma}{r_{ij}} \right)^{6} \right], \tag{9}$$

where ε is the depth of the potential well and σ is the shortest distance at which the potential is zero. To illustrate, an example of this potential is shown in Fig. 5. A potential value to the left of the well results in repulsion, while a value to the right results in attraction between the two atoms. This means that there is an optimum distance at which two neighboring atoms will stay, corresponding to the global minimum of the potential. This is the basis for the formation of crystalline lattices in atomic systems, where all atoms ideally settle at the same distances and angles from their neighbors.

However, a pair potential cannot accurately describe more complicated crystal structures such as the diamond structure common to semiconductors. The addition of a third atom k makes the computation much more complicated, but it allows the representation of a wider variety of systems. When simulating group IV semiconductors, a frequently used three-body potential is the Stillinger-Weber potential [51]. Its formalism is somewhat more complex than that of the Lennard-Jones potential:

$$f_2(r_{ij}) = \begin{cases} A(Br^{-p} - r^{-q}\exp[(r-a)^{-1}], & r_{ij} < a \\ 0, & r_{ij} \geq a \end{cases} \tag{10}$$

$$f_3(\mathbf{r}_i, \mathbf{r}_j, \mathbf{r}_k) = h(r_{ij}, r_{ik}, \theta_{jik}) + h(r_{ji}, r_{jk}, \theta_{ijk}) + h(r_{ki}, r_{kj}, \theta_{ikj}), \tag{11}$$

where

$$h(r_{ij}, r_{ik}, \theta_{jik}) = \lambda \exp[\gamma(r_{ij}-a)^{-1} + \gamma(r_{ik}-a)^{-1}] \times (\cos\theta_{jik} + \frac{1}{3})^2. \tag{12}$$

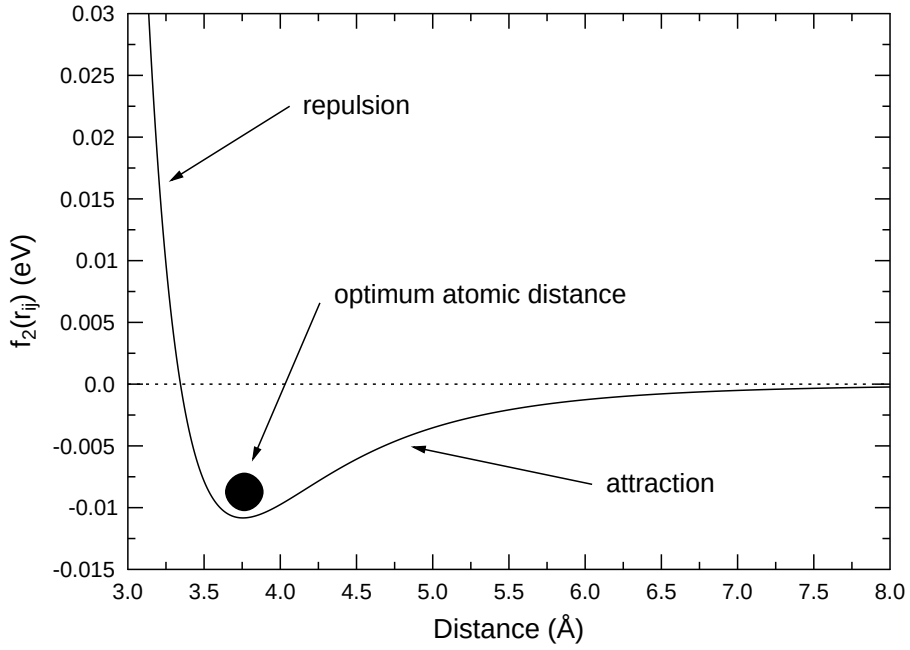

Figure 5: The Lennard-Jones potential for argon with $\varepsilon/k_B = 125.7$ K and $\sigma = 3.345$ Å [50]. The black circle represents an atom at the bottom of the potential well.

In the three-body term, θ_{ijk} is the angle formed at j by the three atoms on their common plane. The potential extends to a *cut-off distance* of length a, where both f_2 and f_3 go to zero naturally. To conform with the dimensions of Eq. 9, the functions f_2 and f_3 are multiplied by an energy unit ε, and a length unit σ is used to normalize the distances.

Another widely used semiconductor potential is the Tersoff potential [52]. Its two- and three-body terms are

$$f_2(r_{ij}) = f(C)(r_{ij})A_{ij}\exp(-\lambda_{ij}r_{ij}), \qquad f_3(r_{ij}) = -f(C)(r_{ij})b_{ij}B_{ij}\exp(-\mu_{ij}r_{ij}), \tag{13}$$

where

$$b_{ij} = \chi_{ij}(1+\beta_i^{n_i}\zeta_{ij}^{n_i})^{-1/2n_i}, \tag{14}$$

$$\zeta_{ij} = \textstyle\sum_{k\neq i,j} f_C(r_{ik})\omega_{ik}g(\theta_{ijk}), \tag{15}$$

$$g(\theta_{ijk}) = 1 + c_i^2/d_i^2 - c_i^2/[d_i^2 + (h_i - \cos\theta_{ijk})^2]. \tag{16}$$

The cut-off function

$$f_C(r_{ij}) = \begin{cases} 1, & r_{ij} < R_{ij} \\ \frac{1}{2} + \frac{1}{2}\cos[\pi(r_{ij}-R_{ij})/(S_{ij}-R_{ij})], & R_{ij} < r_{ij} < S_{ij} \\ 0, & r_{ij} > S_{ij} \end{cases} \tag{17}$$

serves to quell the potential smoothly in the short ($\sim$0.3 Å) interval from R_{ij} to S_{ij}. All other parameters are simply constants that have been discovered by fitting to well-established experimental or quantum-mechanical data.

Like any physical model, interatomic potentials only approximate real interactions to no more than the best of our knowledge. Fitting a potential with a finite set of parameters to accurately describe a specific set of behaviors means that foretelling any behavior not included in this set is by no means guaranteed. For example, the Tersoff potential, originally fit to match experimental values for cohesive energies, lattice constants and elastic constants, overestimates the melting point of Si by about 700 K; the Stillinger-Weber potential does the same for Ge by about 1700 K [41]. Thus, a potential is at best a limited interface between the real world and its representation in the neighborhood of the potential's original purpose. In this neighborhood, however, results are usually good enough to accurately describe similar experimental processes.

4.2 Semi-grand-canonical Monte Carlo

In publication **II**, the MD program Lammps is used instead of Parcas for the sole reason of the relative ease of adding supplementary algorithms to the former. A new Monte Carlo algorithm was written to work in the semi-grand-canonical ensemble to facilitate the migration of particles of a specific element. This semi-grand-canonical Monte Carlo (SGCMC) algorithm worked in conjunction with the classical MD algorithm to produce results not attainable with only the classical method.

4.2.1 Statistical ensembles

In mathematical physics, a *statistical ensemble* is an imaginary set comprising a large amount of quasi-duplicate systems, each of which represents a possible state that accurately depicts a real system. An ensemble is characterized by certain statistical values which depict the average behavior of the particles in the system but lack the information of specific arrangement. These values are pressure p, volume V, number of particles N, temperature T, energy E, and in some ensembles, chemical potential μ. Constraints on different combinations of these values result in different system behaviors, which are classified into a number of different types of ensembles.

A *canonical* ensemble is one where the values N, V, and T are conserved — it is thus also referred to as an NVT ensemble. Similarly, an NVE ensemble is called a *microcanonical* ensemble, and an NpT ensemble is called *isothermal-isobaric*. The constraints μVT make

an ensemble *grand-canonical*; as opposed to the previous ensembles, N is not restricted in the grand-canonical, meaning that the number of particles may change to satisfy the other constraints. The choice of ensemble depends on the goal of the simulation as well as the type of system, and is by no means a trivial matter.

With an additional constraint, a multielemental grand-canonical ensemble can be transformed into a *semi-grand-canonical ensemble*, wherein the total number of particles is conserved, but the chemical potential difference $\Delta\mu = \mu_A - \mu_B$ of two particle species A and B is kept an independent variable [53]. In practice, this means that an atom of type A can be transformed into an atom of type B, and vice versa. Furthermore, fixing $\Delta\mu$ means that N_A and N_B fluctuate around values that satisfy the semi-grand-canonical constraint, and a string of atom type exchanges can be construed as diffusive migration.

4.2.2 The SGCMC algorithm

As opposed to MD simulations, Monte Carlo simulations are, as the name suggests, methods wherein chance plays a significant role. This does not mean that the results of Monte Carlo research are completely random; while the outcome of a single event may be up to chance, the simulations contain such a large amount of individual events that the end result is based on the convergence of a sufficient amount of statistics.

Computers lack the creativity to produce truly random events. Instead, Monte Carlo simulations employ *pseudo-random* numbers, which can be created through a synergy of mathematical and computerized methods as extremely long lists of consecutive, non-sequential numbers. The key to these lists is a *seed number* that must be changed for the outcome of each simulation to be different. Some programs may take their seed number from the last digits of a computer's internal clock (in today's computers, nanoseconds), but for the sake of repeatability, it is best to set the number manually.

In the SGCMC simulation, random numbers are used to determine whether or not to switch atom types. The algorithm is applied a number of times at specified intervals during an otherwise ordinary MD simulation. At each application, the type of a chosen atom is temporarily swapped (from type A to type B or vice versa), and the consequent change in energy of the system is determined. If there is a reduction in energy greater than $\Delta\mu$, the swap is made permanent; if not, the swap persists only if

$$\exp\left(-\frac{\Delta E \pm \Delta\mu}{k_B T}\right) > N_{rand}, \tag{18}$$

where ΔE is the change in energy of the system after the swap, k_B the Boltzmann constant, T the temperature of the simulation and N_{rand} a computer-generated random number between 0 and 1. The sign in front of $\Delta\mu$ indicates the direction of the swap. After a successful swap, the velocity of the atom is rescaled to conserve its kinetic energy.

4.3 Transmission electron microscope image simulations

In experimental physics, the preparation of samples is followed by their characterization using one or more techniques. At the nanoscale, optical inspection, such as with a traditional light microscope, is impossible; instead, there is a multitude of methods at the disposal of scientists who want to characterize their nanoscale samples in two or three dimensions. One very common alternative is electron microscopy in its many forms.

The results of MD simulations are to be comparable with experimental work, which cannot be determined unless there is a common platform for comparison. Transmission electron microscopy (TEM) offers such a platform in that samples simulated through MD can be used further to simulate TEM images. This constitutes one of the few directly observable links between nanoscale computational and experimental physics.

In this study, image simulations are performed for publications **III** and **IV** using the program EMS [54].

4.3.1 Electron microscopy

The electron microscope was conceived and first built by Max Knoll and Ernst Ruska at the beginning of the 1930s [55; 56; 57; 58]. It allows much greater magnification than an optical microscope because an electron's de Broglie wavelength ($\sim 10^{-12}$ m for accelerated electrons) is orders of magnitude smaller than the wavelength of visible light ($\sim 10^{-6}$ m). Therefore, electrons can export information from a sample at a much smaller scale than photons — even at the atomic level.

After 80 years of development, an electron microscope can now take one of many forms; the original method is transmission electron microscopy (TEM), depicted in Fig. 6. A beam of electrons is accelerated, focused, and then transmitted through a thin specimen, where they undergo interactions with the local atoms and emerge carrying information about the structure of the sample. They are then caught onto a phosphorous screen, where an image containing this information is formed. Various focusing and lensing efforts can lead to coherent images

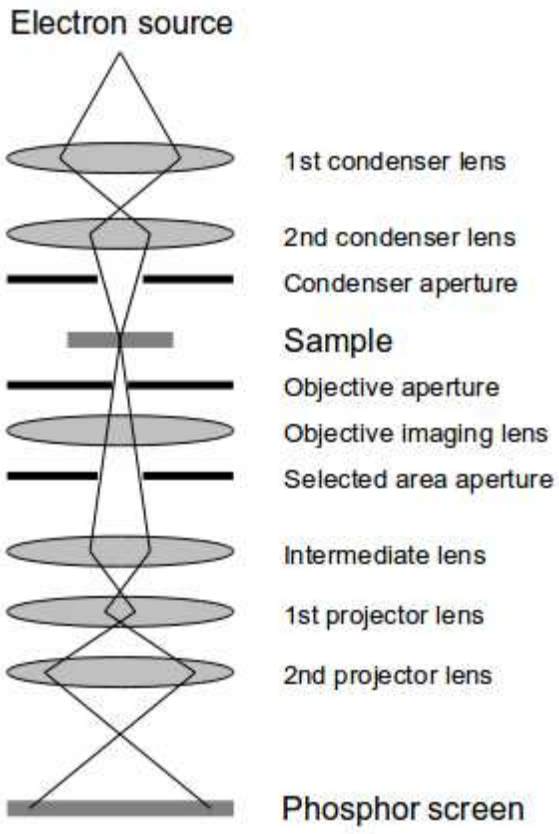

Figure 6: A schematic view of an electron microscope.

with enough magnification to surpass all optical microscopes, even to the point of distinguishing individual atoms.

Contrast in a TEM image is formed through differences in the amplitude of the electron beam at each spot on the imaging plane. These differences can be caused by two things: the absorption of electrons into the sample, and interference caused by phase shifts incurred by transmitted electrons. In conventional transmission electron microscopy (CTEM), only the amplitude of the exiting electron beam is investigated, meaning that projected paths along which more electrons have been absorbed are darker than those where the electrons have a better chance to pass through the entire sample. This makes CTEM imaging quite comparable to radiography, where the same process is used with X-rays instead of electrons. Using this method, it is not possible to reach atomic resolution, which can only be achieved using high-resolution transmission electron microscopy (HRTEM), where the interference caused by differences in phase of the beam electrons is investigated instead; this adds the requirement of making the imaged specimen extremely thin to avoid phase shifts over multiple periods.

The majority of electrons pass through the specimen in a more or less straight line. Thus,

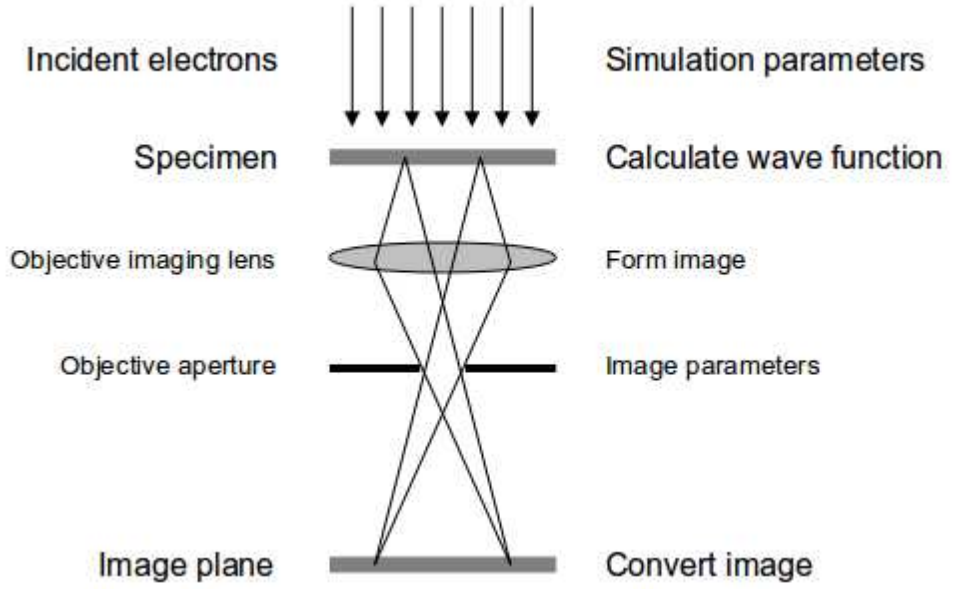

Figure 7: A simplified schematic of an electron microscope (left labels) and the translation into an image simulation (right labels).

the image containing the most information is formed on a plane perpendicular to the original beam centered on its path. This kind of image is called *bright-field* due to the large amount of impinging electrons. However, due to the wave-particle duality of electrons, their passing through a crystalline sample also forms a diffraction pattern locatable at several points not on the beam path. An image formed at one of these locations is called *dark-field* [59].

4.3.2 Modeling a TEM image

Fig. 7 shows what basic elements of a TEM must be considered when making a simulation of the imaging process. The simulation begins with the formation of the electron wave function $\psi_f(x, y, z)$ which satisfies the Schrödinger equation in an electrostatic potential $V(x, y, z)$:

$$\left[-\frac{\hbar^2}{2m}\nabla^2 - eV(x, y, z)\right]\psi_f(x, y, z) = E\psi_f(x, y, z), \tag{19}$$

where $e = |e|$ is the electric charge of the electron and E its total energy, which in an electron microscope can be approximated as the kinetic energy since it is much greater than any potential energy gain or loss within the sample $(-eV)$ [60]. One solution of the equation is of the form

$$\psi_f(x, y, z) = \psi(x, y, z)\exp(2\pi i z/\lambda), \tag{20}$$

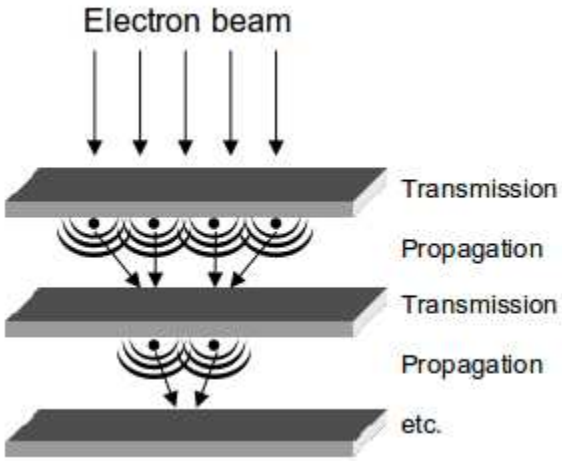

Figure 8: The principle of the multislice technique.

where λ is the electron wavelength. The wave function has been separated into the product of a plane wave propagating in the z-direction and $\psi(x, y, z)$, the reduction of the wave function into the xy-plane where any further variation in z is minimal.

As the electron beam propagates through a thin specimen, it interacts with the atomic potential, causing a phase shift in the plane wave. This means that depending on what an individual electron encounters within the sample, it will either exit in a different phase compared to undisturbed electrons or be absorbed completely into the sample. Since the imaging process in HRTEM is sensitive to the phase of the impinging electrons, this results in an amount of contrast in simulated images that makes it possible to distinguish between different types and amounts of atoms on electron paths along the z-axis, projected as points onto the xy-plane that form the pixels of a computerized image.

Calculating how the wavefunction evolves during its passage through a sample is relatively straightforward for very thin specimens, but it can become very CPU-intensive as the thickness of the sample increases, due to *e.g.* the increased possibilities of scattering in thicker specimens. A way around this problem is to divide the specimen into a number of thin slices along the path of the electron beam, and then treat the whole sample as a collection of consecutive slices separated by void [61; 62]. This so-called *multislice* technique, pictured in Fig. 8, makes it possible to simulate TEM images of samples with realistic thicknesses to produce results comparable to experimental ones [63; 64].

The thickness of an individual slice is a simulation parameter that has more of an effect on simulation time than on the end result itself. However, parameters that have an actual impact

on the appearance of the simulated image include electron wavelength (set through the electron beam energy), objective aperture, spherical aberration, and defocus. The higher the beam energy, the lower the electron wavelength, which improves the resolution of the image; this value is typically of the order of 40–400 keV in experimental work. The objective aperture is used to limit the amount of electrons used for forming the image; too large an aperture saturates the imaging device while too small an aperture results in a completely dark image. Spherical aberration occurs due to imperfections in magnetic lenses and cannot be entirely avoided, although successful attempts have been made at reducing its effect in recent years [65]. Defocus is used to correct the effects of aberration when imaging diffracted beams, and is therefore unnecessary in bright-field imaging.

5 CHARACTERIZATION METHODS

In computer simulations, clusters are nothing more than lists of atomic coordinates. Visualization programs can use these lists to form pictures of the clusters in question as shown back in Fig. 3. However, the majority of relevant information must be extracted indirectly. MD simulations modify the lists over time in a way that may not be visible in pictures, but that can have a drastic effect on values computed from the coordinates. Adherence to given potentials ensures that the simulations strive to optimize the *free energy* of the system as calculated as a function of the potential.

The Helmholtz free energy F is defined as

$$F = E - TS, \tag{21}$$

where the total internal energy $E = E_{kin} + E_{pot}$ is the sum of the kinetic and potential energies of the system, T is the temperature, and S the entropy. In statistical mechanics, entropy can be defined as

$$S = k_B \ln \Omega, \tag{22}$$

where k_B is the Boltzmann constant and Ω the number of possible states that satisfy the given statistical values of an ensemble as described in Sect. 4.2.1 [66; 67]. This definition follows from the general (Gibbs) entropy for a collection of equally probable states [68]. In a closed system, any change in entropy must always be non-negative; this translates into an increase in the number of possible states, or an increase in disorder. A system where entropy is maximized is said to be in *thermal equilibrium*.

In classical thermodynamics, where individual particles are ignored in favor of average properties, the change in entropy of a system as it absorbs a small amount of heat δQ is

$$\Delta S = \frac{\delta Q}{T}. \tag{23}$$

While individual atoms are the basis of MD simulations, the number of atoms in the simulated systems is large enough for the calculation of these average properties to be sensible. It is thus correct to use relations such as Eq. 23 when describing the behavior of free energy in these systems.

Consider a canonical (NVT) ensemble, where the temperature is kept constant with an external heat bath. In an MD simulation, this can be achieved with a temperature control algorithm

applied to atoms in the immediate vicinity of the periodic cell borders [69]. Therefore, assuming no work is being done by the system, any potential energy released as heat during the simulation is transferred to the heat bath, changing its entropy by

$$\Delta S_{ext} = -\frac{\Delta E_{pot}}{T}, \tag{24}$$

since E_{kin} is a function of temperature and thus stays constant. For the same reason, differentiating Eq. 21 gives the simple relation $\Delta F = \Delta E_{pot} - T\Delta S_{int}$, which when combined with Eq. 24 yields

$$\Delta S_{tot} = \Delta S_{ext} + \Delta S_{int} = -\frac{\Delta E_{pot} - T\Delta S_{int}}{T} = -\frac{\Delta F}{T}. \tag{25}$$

Since $\Delta S_{tot} \geq 0$, it is clear from this equation that the free energy of the system must decrease ($\Delta F \leq 0$) in any process simulated in the canonical regime. This usually implies a decrease in potential energy and an increase in entropy, or a change in the state of the system that draws it closer to equilibrium — however, in some cases, *e.g.* phase transitions, it is possible for E_{pot} to increase if the product $T\Delta S_{int}$ increases more.

5.1 Cluster characterization

Free energy is a measure of how well a cluster is formed. An ideal cluster stores a minimal amount of potential energy and is in a state of equilibrium, which by definition means that its entropy is maximized. A perfect free energy value for a given kind of cluster thus exists, and any deviation from perfection translates into an elevated free energy. Such deviations imply that the cluster atoms are somehow misplaced.

Entropy cannot be calculated from a list of atom coordinates in the same way as potential energy. Fortunately, the two values are linked in that the displacement of atoms affects them in a commensurate way. Therefore, keeping track of the energy of the system is a sufficient way to gauge the effect of a simulation, and all changes occurring during the simulation can be judged in terms of their effect on the potential energy.

5.1.1 Sphericity

The definition of the perfect cluster shape varies with size. At the lower nanoscale, where the effective size of an atom can be of the same order of magnitude as that of the entire cluster,

it is impossible to construct a perfect sphere of atoms. In fact, below a certain size limit, atoms tend to aggregate into non-spherical clusters containing a very specific number of atoms, called a *magic number* [70]. In very small clusters (less than about 50 atoms), these numbers correspond to completed levels within the electronic shell structure [71; 72]; whereas in larger clusters, this effect is overshadowed by geometric considerations that cause the clusters to form perfect polyhedral shapes [73]. These configurations are so favorable that, as compared to clusters with a different number of atoms, they are formed in a relative abundance that starts as very high with small clusters and decreases as the size of the cluster grows.

When the cluster contains many hundreds of atoms or more, occupying a polyhedral face becomes energetically tolerable and the cluster shapes start to resemble spheres. When this is the case, the ideal sphere can be taken as a model structure, from which any deviation can be assumed to bind potential energy. Thus, characterizing a cluster by its measure of *sphericity* gives information about how far the cluster is from equilibrium.

Sphericity was originally defined as the ratio of the surface area of a sphere to the surface area of a particle having the same volume as the sphere in question [74]. This definition is not practical for MD simulation purposes because there is no unambiguous way to define the surface area of a discrete system of atoms. Instead, sphericity is redefined in this study as $S = V_c/V_{max}$, where

$$V_c = \sum_i \frac{N_i}{\rho_i} \tag{26}$$

is the total volume taken up by a cluster having N atoms of elements i with densities of ρ_i, and

$$V_{max} = \frac{4}{3}\pi r_{max}^3 \tag{27}$$

is the volume encompassed by a hypothetical spherical cluster with the same radius as the maximum atom distance r_{max} from the center of mass of the actual cluster. Thus, a perfect sphere has $S = 1.0$; a very flat and elongated ellipsoid has $S \to 0$; and an actual simulated cluster falls somewhere in between.

5.1.2 Crystallinity

As shown in Section 4.1.2, there is an optimum interatomic distance at which the potential energy between two atoms is at its lowest. The only way that all atoms in a system can be at this distance from their neighbors is if they form a *crystalline* periodic lattice. This is why a number of materials (usually semiconductors, metals, and compounds thereof) tend to be

crystalline at the bulk level. This tendency extends all the way down to the nanoscale, which means that a perfect nanocluster is also crystalline.

Crystallinity in numerical samples can be quantified with the help of a *structure parameter* defined as

$$\begin{aligned} P_{st}(i) &= \frac{1}{p_u(i)} \left(\sum_j (\theta_i(j) - \theta_i^p(j))^2 \right)^{1/2} \\ p_u(i) &= \left(\sum_j (\theta_i^u(j) - \theta_i^p(j))^2 \right)^{1/2} \end{aligned} \tag{28}$$

where $\theta_i(j)$ is a list of the $n_{nb}(n_{nb}-1)/2$ angles formed between atom i and its n_{nb} nearest neighbors; the number n_{nb} is determined from the ideal crystal structure, and is 4 for the diamond structure (which applies to both Si and Ge); $\theta_i^p(j)$ is the distribution of angles in a perfect lattice; and $\theta_i^u(j) = j\pi/n_{nb}(n_{nb}-1)/2$ is the uniform angular distribution [75]. Thus, all atoms of a perfectly crystalline lattice at 0 K have a value of $P_{st} = 0$, whereas any deviation results in a distribution with a peak somewhere between 0 and 1. However, for temperatures above 0 K, atoms are mobile in the vicinity of their ideal location, and for any "freeze frame" list of coordinates, the angular distribution is worse than a distribution built from coordinates averaged over time.

5.1.3 Elemental segregation

Experimental work has shown that in a cluster containing atoms of more than one element, there is a preferential relative location for each type of atom [76; 77]. This effect can be reproduced with MD simulations using bimetallic clusters [70] or even silicon and germanium [78]. In the case of the latter, Ge atoms have a tendency to segregate to the surface of the cluster. This is due to the lower surface energy of Ge as compared to Si [79], which makes this atomic configuration energetically advantageous. It is also intuitively clear that since Ge atoms occupy a larger volume than Si atoms, their preferred location is on the surface.

Elemental segregation in simulated clusters can be investigated simply by calculating the average distance of each type of atom from the center of mass of the cluster. By graphing these distances as a function of simulation time, the segregation effect can be seen as a direct result of the application of an interatomic potential to a non-ideal starting configuration.

5.2 Layer characterization

In the research carried out for this thesis, two different kinds of clusters were simulated: to study their formation process and structure, clusters were condensed from an atomic vapor; and to study deposition, clusters were cut out from a crystalline bulk. This difference is mainly due to the order of the research, although the clusters achieved through simulated condensation never did reach a form close enough to equilibrium to be considered for use in deposition simulations. As such, the quantities described in Sect. 5.1 are irrelevant to that part of the study where deposition is concerned.

Instead, the two main ways in which the deposited layers were analyzed have more of a practical undertone. The first is the determination of the layer's porosity P, or alternatively its density profile. These effectively mean the same thing, although porosity is the value more frequently used to describe layers of porous silicon. In this thesis, this value was defined as

$$P = 1 - \frac{Na^3}{N_0 V}, \tag{29}$$

where N is the total number of atoms in the layer, a the lattice constant of the deposited element, N_0 the number of atoms in a unit cell of this element, and V the total volume of the layer. In these simulations, the number of deposited clusters was so small that the roughness of the surface was enough to cause an ambiguity in the volume of the layer. This is why two different porosities were defined using two different volumes: the maximum porosity $P_{max}(V_{max})$ using the cuboid limited by the periodic boundaries of the simulation cell and the height coordinate of the highest deposited atom; and the minimum porosity $P_{min}(V_{min})$ using an integrated volume where the height was defined locally by the highest atom coordinate in a small area, thus approximating the layer's surface [80]. When compared to the total layer volume, the relative difference of these two values decreases as the layer grows, but in these simulations, the difference is substantial, and the "real" porosity is a value between the two.

The second way to analyze deposited layers is using TEM image simulations. TEM images are sensitive to the electronic structure of the imaged sample, which is affected among other things by strain caused by anything from misplaced atoms to elemental interfaces, *i.e.* any atomic configuration that differs from crystalline bulk. Also, the electronic structure of bulk materials differs from element to element. These differences result in image contrast that can make individual clusters visible and allows to differentiate between clusters of different elements. These features make TEM images a perfect tool to study cluster-deposited layers where the conservation of crystallinity of the original clusters is a critical issue.

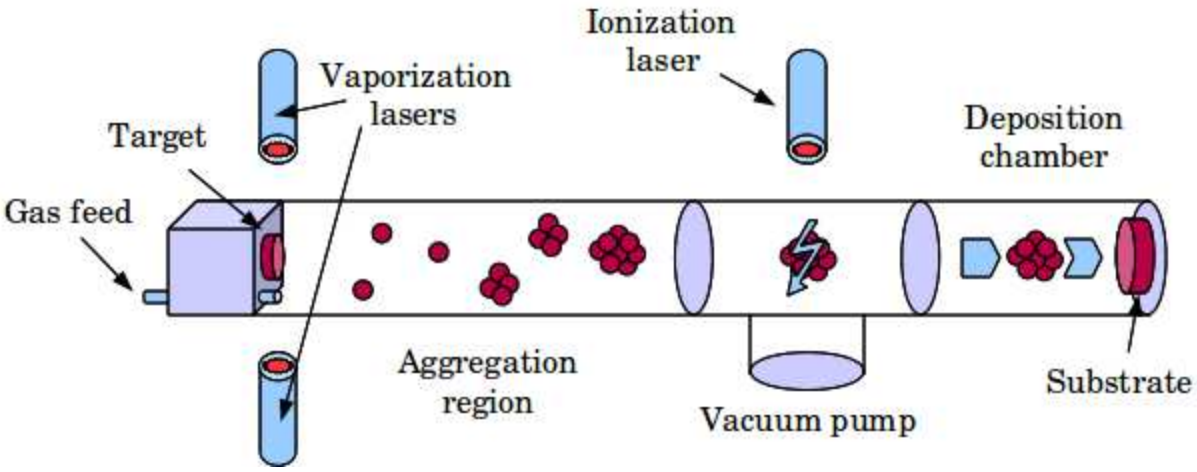

Figure 9: The schematic layout of a cluster deposition apparatus. Heating or magnetron sputtering sources, where the required elements are connected to the target, do not require vaporization lasers. The ionization laser is also supplementary as it is not needed in LECBD.

6 THE PATH TO A POROUS MULTILAYER

A typical cluster deposition apparatus is outlined in Fig. 9. There are several different methods commonly used to obtain individual atoms for cluster formation (*e.g.* direct heating [81; 82], laser vaporization [83], magnetron sputtering [84]). These atoms are ejected from a target consisting of the desired cluster material and swept by an aggregation gas such as helium or argon along the aggregation region, where the inert gas facilitates the nucleation of clusters by absorbing excess kinetic energy, making the vapor supersaturated. The mean size of the clusters thus condensed can be controlled by modulating the particle flux from the source, the gas temperature and pressure within the aggregation region, and the time allowed for condensation (or length of the aggregation region).

After condensation, the clusters can be ionized for acceleration, although this is not necessary for low-energy deposition. Non-ionized clusters gain enough momentum from the exhaust of the aggregation gas from the higher pressure of the cluster source into the vacuum outside it, and they reach the substrate before gravity can have any significant effect. Once on the substrate, the clusters are bound to the surface atoms and remain there to form films as more clusters are deposited.

6.1 Publication I: Cluster condensation

To model the formation of clusters as described above, a simplification has to be made: regardless of the type of source, a continuous flow of individual atoms can be supplied. As the principles of atom sputtering hold very few secrets, this is a safe assumption that gives a starting point for computational work: the simple combination of cluster atoms and aggregation gas atoms in vaporous form. In this case, the elements in question are Si, Ge, and Ar.

The required simulation cell contains a random distribution of specific numbers of these three types of atoms, separated by a minimum distance greater than the potential's cut-off distance. The aggregation gas pressure is defined as a constant value by having the same amount of Ar atoms in each cell, the volume of which is kept fixed throughout the simulation. This means that the sum of Si and Ge atoms is constant, but their respective amounts can be changed to obtain a Si_xGe_{1-x} cluster with a variable x. The gas pressure (12.5 bar) is many orders of magnitude higher than in experimental deposition (*e.g.* 10^{-3} mbar [85]); this has the effect of increasing the frequency of atomic collisions in the system, thus making the simulations quicker.

During a simulation, the atoms travel around the simulation cell until they encounter other atoms. Because of the shape of the potentials, when two semiconductor atoms and at least one other atom of any kind meet, the semiconductor atoms are likely to stay together, whereas all Ar atoms are repulsed. Forming a bond releases energy, which causes recently bonded atoms to move faster, raising the kinetic energy and thus the temperature of the system. Since the system is in a simulated heat bath as described in Sect. 5, this energy is gradually removed from the system through interactions with the Ar atoms. This behavior continues until all semiconductor atoms in the cell are part of the same cluster, which cools down to the desired temperature set at the beginning of the simulation (300 K), evident in Fig. 10.

The condensation into a single cluster is due to the confined nature of a simulation cell that uses periodic boundaries. With these boundaries, the simulation is meant to realistically represent the development of an atomic vapor: as the size of the clusters in an experimental cluster beam increases, the space between them increases as well, and the possibility of further agglomeration decreases. In simulations, this forcedly results in an exact cluster size, since all atoms in the system eventually encounter each other; whereas in experiments, it leads to a Gaussian size distribution around a certain mean value dictated by the experimental parameters, as long as the clusters are large enough to avoid the aforementioned magic numbers.

When small agglomerates collide during the cluster formation process, the released surface energy is usually enough to nudge the atoms into positions required to form a new, larger

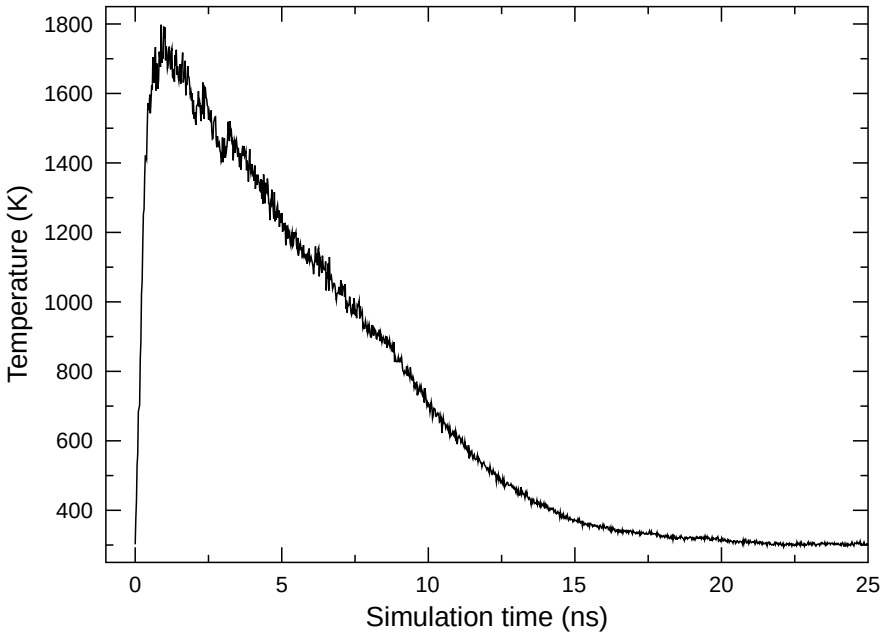

Figure 10: The system temperature during a cluster condensation simulation.

sphere. However, the bigger the constituent agglomerates, the more energy is needed and the more difficult this becomes, until the energy stored in the agglomerates alone is no longer sufficient to produce a spherical shape during the initial stages of cluster formation. This effect is visible in the simulations as clusters that clearly consist of separate spherical parts that have not melded into a single sphere. Examples of both kinds of clusters are shown in Fig. 11.

The fact that the simulation results contain a majority of single spherical or near-spherical clusters as well as several of these "multispherical" clusters suggests a difference in collision conditions between these end results. As the graph in Fig. 10 shows, the later the collisions take place, the lower the system temperature has fallen due to the heat bath, and therefore, the less energy is available for atomic movement. This could imply that the malformed clusters were too slow to become fully spherical, falling victim to rapid temperature scaling; but if this were a real problem, simulations run at the higher base temperature of 600 K should yield a better average sphericity, which is not the case.

Judging from experimental results [29; 32], clusters can be expected to become crystalline at least within the time that they can be observed experimentally. Investigating the structure parameter distribution described in Sect. 5.1 and depicted in Fig. 12 shows that the condition of crystallinity defined by the original author (a distribution peak below 0.2 [75]) is satisfied by all simulated clusters regardless of their sphericity. This does not mean that the clusters are perfectly crystalline; rather, it implies that they contain nanocrystalline regions that are

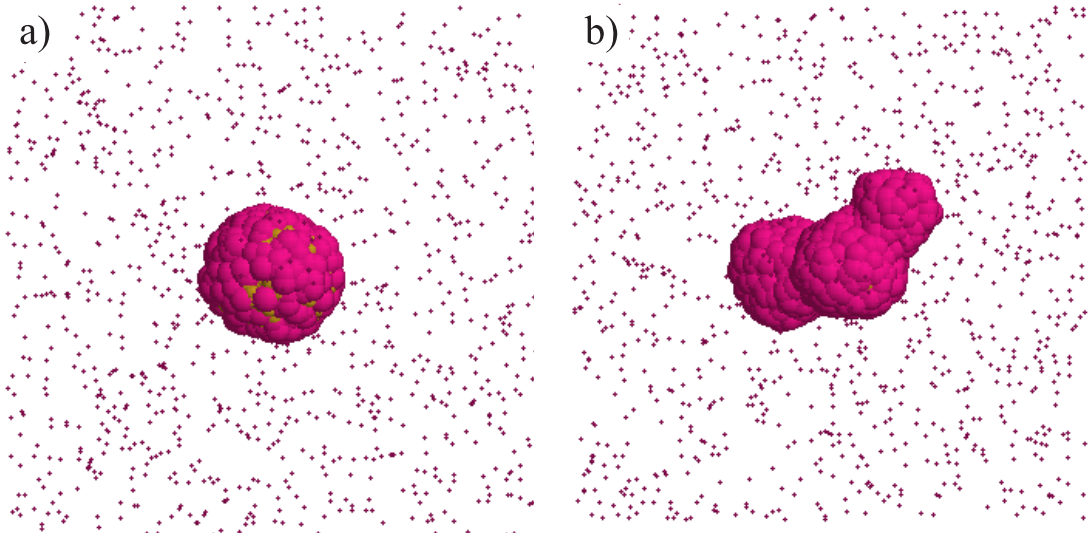

Figure 11: The visualization of a) a cluster of $Si_{0.8}Ge_{0.2}$ and b) three attached clusters of $Si_{0.2}Ge_{0.8}$ floating in an Ar atmosphere. From publication **I**.

not perfectly aligned with each other, and that aligning them any further would shift the peak closer to zero.

Elemental segregation is also clearly visible in the freshly condensed clusters when using the Stillinger-Weber potential; however, it is debatable whether the Tersoff simulations produce any segregation whatsoever. In the average distance graphs shown in Fig. 13, Ge atoms in the Tersoff simulations remain at a constant average distance from the center of mass of the cluster regardless of their amount, which means that their position within the cluster is random. Only the fact that this average distance is clearly higher for Ge atoms than for Si atoms shows that there is a tendency for the Ge atoms to settle further away from the center. This behavior is markedly different from the Stillinger-Weber simulations, where the average distance drops as a function of Ge atom percentage. This suggests that with smaller concentrations, the Ge atoms are occupying space close to the surface, and that there is no room for additional atoms, which are forced to settle closer to the center as the Ge concentration increases.

These results represent clusters within nanoseconds of their formation. It is clear from the lack of perfect sphericity, crystallinity, and elemental arrangement that thermal equilibrium has not been reached. One would expect experimental clusters to be much closer to such a state, which could hypothetically be proven with an infinitely long MD simulation using an infallible interatomic potential. Failing that, setting different MD parameters or using an altogether different simulation method can be the next best thing.

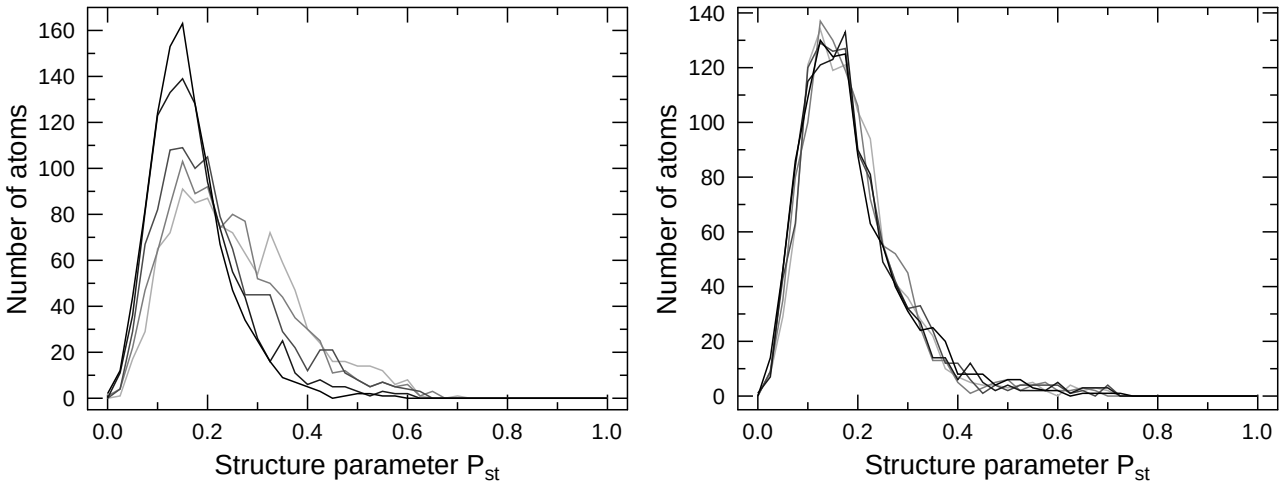

Figure 12: The distribution of the structure parameter P_{st} in the condensed clusters using the Stillinger-Weber (left) and the Tersoff (right) potentials. The darker the line, the higher the Ge concentration. From publication **I**.

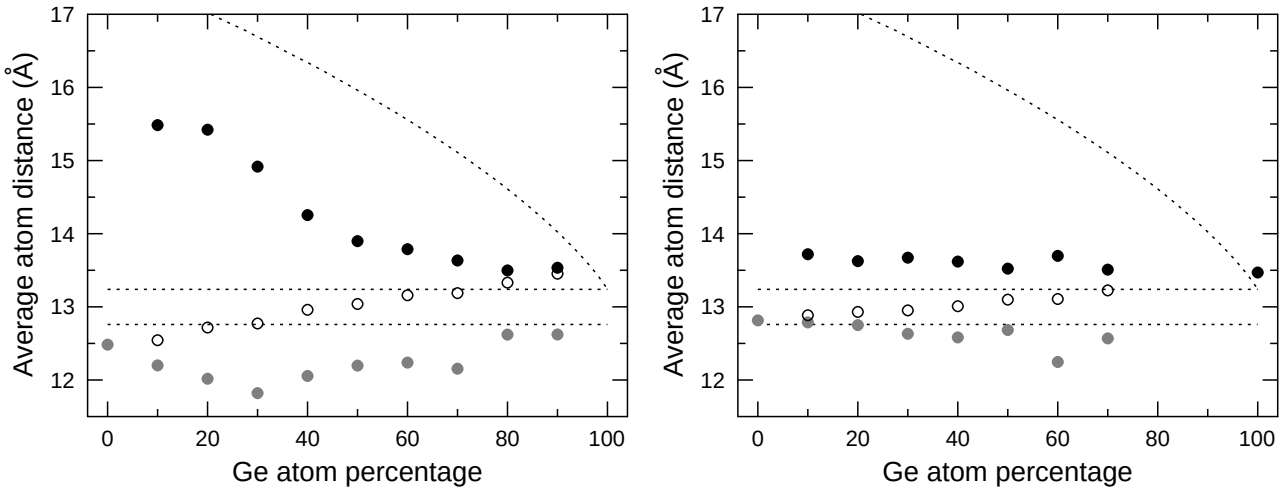

Figure 13: Average distances of Si (grey) and Ge (black) atoms from the center of mass of the cluster using the Stillinger-Weber (left) and the Tersoff (right) potentials. The empty circles denote average distances of both Si and Ge atoms combined; the horizontal dotted lines represent the average atom distances for perfect clusters of Si (lower line) and Ge (higher line); the curved dotted line represents the average distance of Ge atoms as a function of percentage in a perfect cluster where the Ge atom distribution starts at the surface of the cluster. From publication **I**.

6.2 Publication II: Structural optimization

The structure of malformed clusters can be further investigated by trying to recreate the conditions favorable to the formation of single spheres. This means raising the temperature to increase the kinetic energy of the atoms, facilitating their movement in a process known as *annealing*. If attaining a high sphericity is simply a matter of prolonging the time during which the clusters have access to a certain amount of energy, then annealing at a temperature close to the highest temperature in the graph of Fig. 10 (*i.e.* 1800 K) should result in spherical clusters; if, on the other hand, there is something more at stake, then something further must be done to optimize the structure of the condensed clusters — something like raising the annealing temperature, or using another simulation method such as SGCMC.

6.2.1 Annealing simulations

Depending on the time scale, there are two mechanisms by which the atomic configurations of clusters may evolve: if enough energy is readily available, the cluster melts, which greatly facilitates the movement of atoms about each other; but if there is no excess energy, the movement of atoms is restricted to within their potential wells, with only the occasional random leap that results in the phenomenon known as *diffusion*. The difference in time scales between these two mechanisms is tremendous: melting and the consequent rearrangement of atoms can easily be observed in MD simulations, while diffusion effects require so much more time that they generally cannot be seen.

In MD simulations, melting is evident as the sudden dissociation from a rigid angular distribution, characterized by an ever-increasing number of defects within the crystalline lattice that slowly loses its integrity [86; 87]. By this definition, a melted cluster cannot be in an ideal structural configuration, since it lacks any aspect of crystallinity. Therefore, after the annealing process, the cluster must be cooled back to its original temperature (300 K) slowly enough to induce a crystalline reformation upon solidifying.

Melting is not a commonly used parameter in potential fitting, which means that the natural melting points of simulated materials are often not correctly reproduced. As mentioned in Sect. 4.1.2, the Tersoff potential overestimates the melting point of Si to about 2400 K (from 1687 K) and the Stillinger-Weber potential that of Ge to about 2900 K (from 1211 K) [41]. This reveals the curious fact that even though the cluster temperatures in the condensation simulations exceeded the natural melting points of both elements, whether or not the simulated clusters were actually molten depended on the potential used as well as the element ratio. Thus,

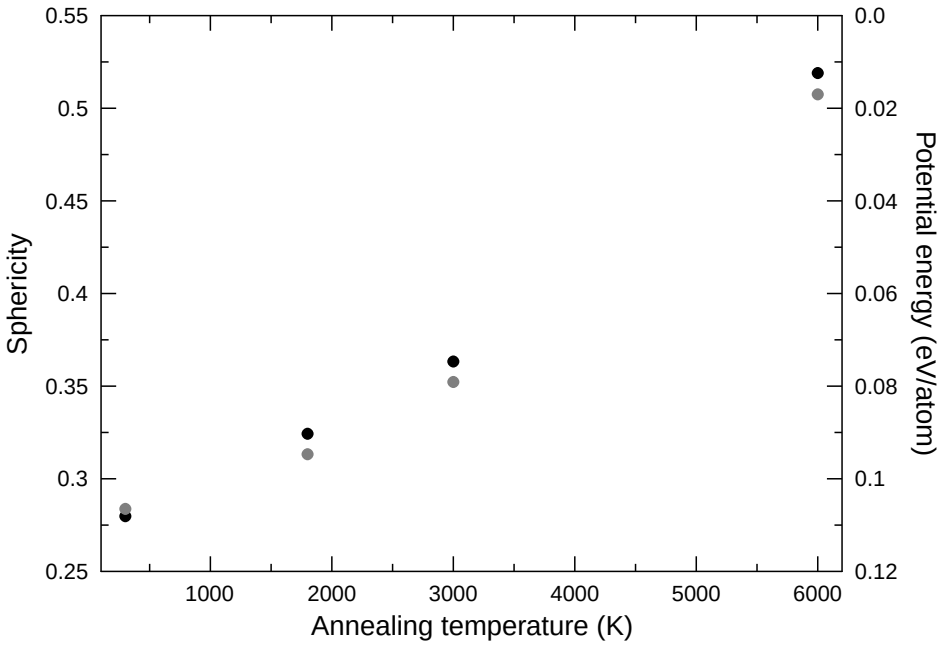

Figure 14: The average effect of annealing temperature on the sphericity (black dots) and the potential energy (grey dots) of a cluster annealed using the Tersoff potential. The potential energy is normalized so that the energy corresponding to a cluster in thermal equilibrium is zero. The data for 300 K represents the values for a cluster prior to annealing.

to instigate melting, a higher annealing temperature has to be used in addition to the 1800 K previously mentioned — say, 3000 K, which is guaranteed to melt all clusters regardless of composition and potential used. If even this is not enough, the maximum temperature that can be used is just below the (potential-defined) boiling point of both elements, which is around 6000 K; however, this temperature is so far removed from the original parameter neighborhood of the potentials that the results cannot necessarily be taken at face value.

The effect of annealing on the multispherical clusters is indeed found to depend on the annealing temperature. The graph of Fig. 14 shows this dependence to be close to linear, even though there is no obvious physical basis for linearity. The proximity of the values in the transposition of their respective coordinates could imply that an average sphericity value much over 0.55 cannot be reached — however, this would be based on the assumption that all of the decrease in the cluster's potential energy is due to an improvement in sphericity, which is not the case. Indeed, it is easy to find clusters that attain a sphericity much closer to unity, as shown in Fig. 15.

Another factor that decreases the energy of a cluster is improved crystallinity. According to Fig. 16, it would seem that annealing at the lower temperatures has only a very slight effect in

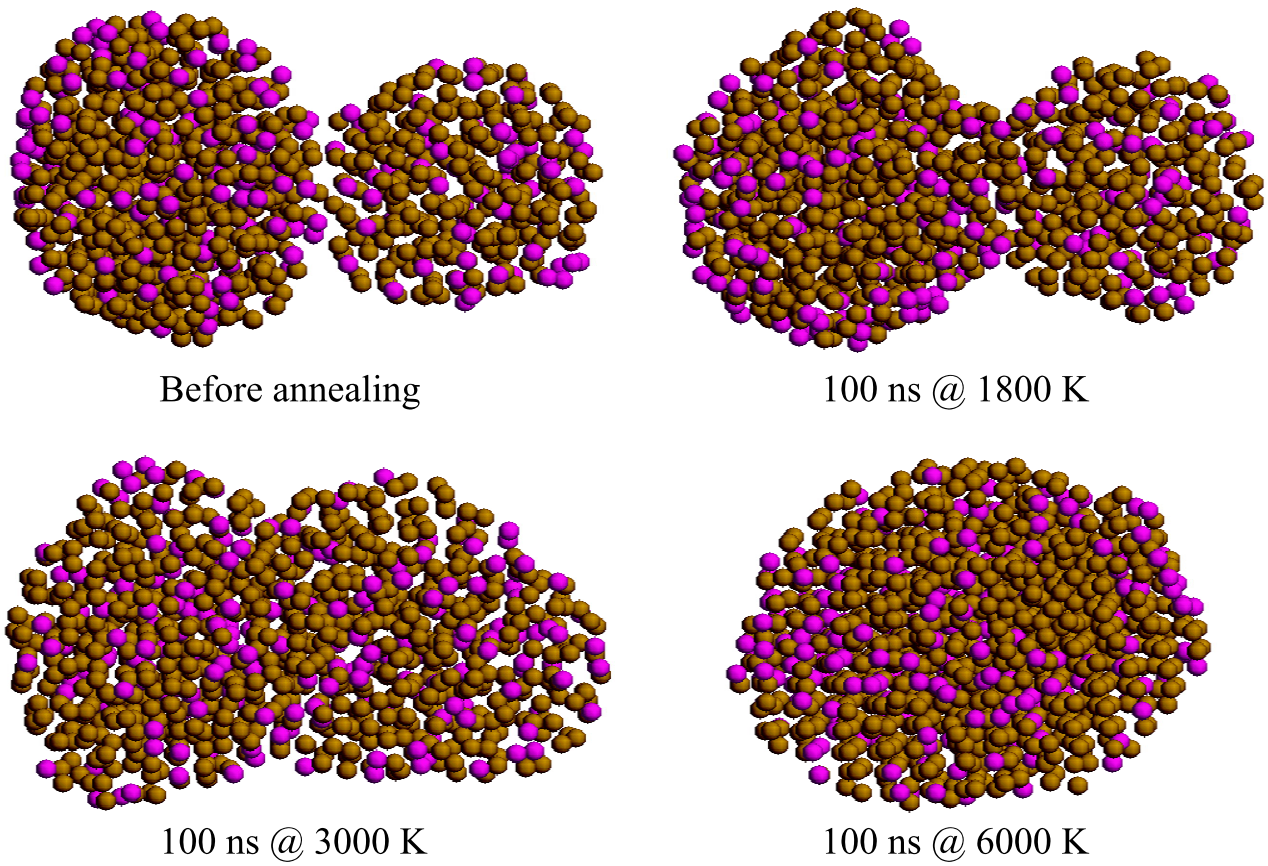

Figure 15: The effect of annealing on the structure of a cluster of $Si_{0.8}Ge_{0.2}$ originally condensed using the Tersoff potential. The sphericities of the clusters are 0.21, 0.23, 0.29, and 0.69 in order of increasing annealing temperature.

improving crystallinity, apparent as a minute leftward shift of the distribution peak. However, annealing at 6000 K successfully aligns the cluster atoms to a crystalline lattice quite comparable to a cluster cut out from bulk. This results in a drop in potential energy from a cause not shared by annealing at 1800 K or 3000 K, disrupting any possible linearity in Fig. 14.

6.2.2 Monte Carlo simulations

Further surface segregation of Ge atoms is not investigated through annealing, since the required diffusion would be extremely slow at any of the lower annealing temperatures. Instead, a new method for facilitating diffusion is introduced: the semi-grand-canonical Monte Carlo routine. It is used primarily to ascertain the general tendency of segregation and its effect on the potential energy of the cluster.

The general phenomenon is investigated using spherical crystalline Si_xGe_{1-x} clusters where the

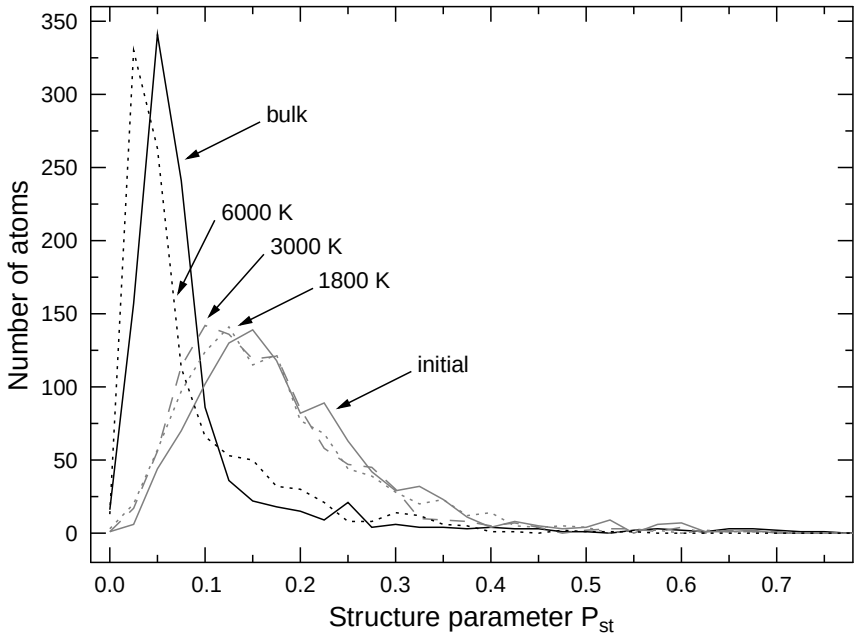

Figure 16: The effect of annealing temperature on the structure parameter P_{st} distribution (crystallinity) of a cluster annealed at 1800 K (grey dotted line), at 3000 K (grey dashed line), and at 6000 K (black dotted line), all using the Tersoff potential. For comparison, the distribution is also shown for a cluster prior to annealing (grey solid line) and a cluster cut out from crystalline bulk and simulated with the SGCMC algorithm (black solid line). From publication **II**.

Ge atoms are placed *inside* the cluster and the Si atoms on the outer layers (*i.e.* the opposite of the energetically favorable configuration). The value of x is set indirectly using the $\Delta\mu$ defined in Sect. 4.2.1; the dependence of one on the other is unknown, and therefore simulations using a large array of different $\Delta\mu$ values first have to be performed to map this dependence as in Fig. 17. The results can then be used as a guide for what value of $\Delta\mu$ to use to achieve a desired element ratio.

The difference in location of the curves for the Tersoff and Stillinger-Weber potentials in Fig. 17 demonstrates how the values can vary depending on the potential from which they are calculated. This brings up a key point: while the observable energetics of an elemental lattice (surface energy, diffusion energy, etc.) can be accurately reproduced using a variety of different potentials, this does not mean that the contribution of an individual atom or a random set thereof is identical regardless of potential. This fact renders incommensurate the results from the two potentials used here, thus preventing any quantitative comparison of the effect of the simulations in this work on the potential energy of the clusters. For this reason, only the results for the Tersoff potential are considered in the publication, a choice prompted by the failings

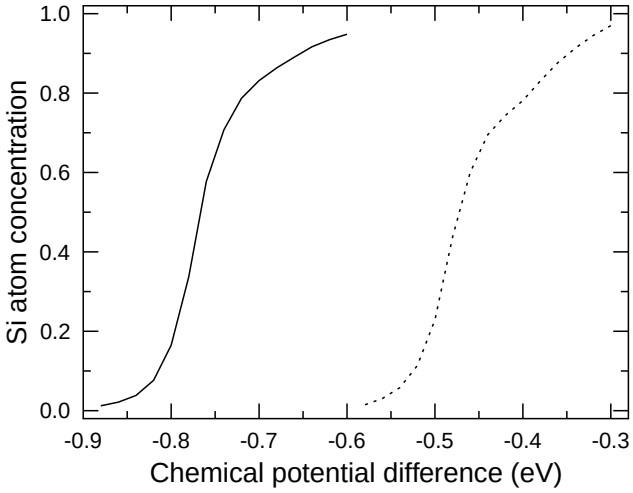

Figure 17: The concentration of Si atoms (or the x in Si_xGe_{1-x}) in a spherical cluster of 943 atoms as a function of $\Delta\mu$ for the Tersoff (solid line) and the Stillinger-Weber (dashed line) potentials.

of the Stillinger-Weber potential to accurately describe the energetics of amorphous Si and Ge [88].

The crystalline sphere simulations show that the Ge atoms migrate to the surface of the cluster rather instantly, as seen in Fig. 18. The values fluctuate close to around 12 Å for Si and just below 14 Å for Ge, which nearly coincides with the values for freshly condensed clusters simulated with the Stillinger-Weber potential in the previous publication (see Fig. 13). This indicates that the elemental segregation in those clusters reached an almost ideal point, which did not happen in the Tersoff simulations. Taking a cluster condensed using the Tersoff potential and further simulating it with the SGCMC algorithm proves this: as Fig. 19 demonstrates, (a) segregation is enhanced and (b) the energy of the system is consequently reduced.

In conjunction with the annealing results, it is thus shown that improvements in sphericity, in crystallinity, and in elemental segregation all contribute to lowering the potential energy — and thereby also the free energy — of a cluster. Of these, sphericity is the hardest to improve: while the mathematical value for sphericity is increased throughout the annealings, this only straightens out the interfaces of the smaller agglomerates, producing clusters with an ellipsoid shape instead of an entirely spherical one, as can be seen in Fig. 15. This indicates that diffusion from stable local minima is extremely difficult even with extreme annealing temperatures.

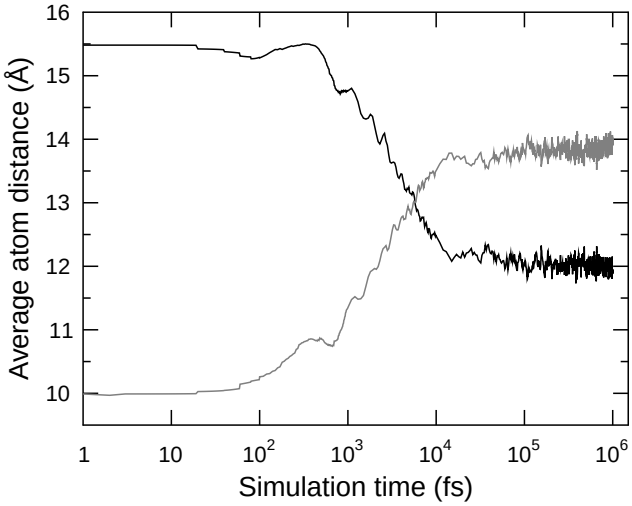

Figure 18: The average atom distance from the center of mass of the cluster for Si (black) and Ge (grey) as a function of simulation time for a spherical cluster of $Si_{0.5}Ge_{0.5}$ cut out from crystalline bulk simulated using the SGCMC algorithm, starting with all Ge atoms inside and all Si atoms on the outer shells. From publication **II**.

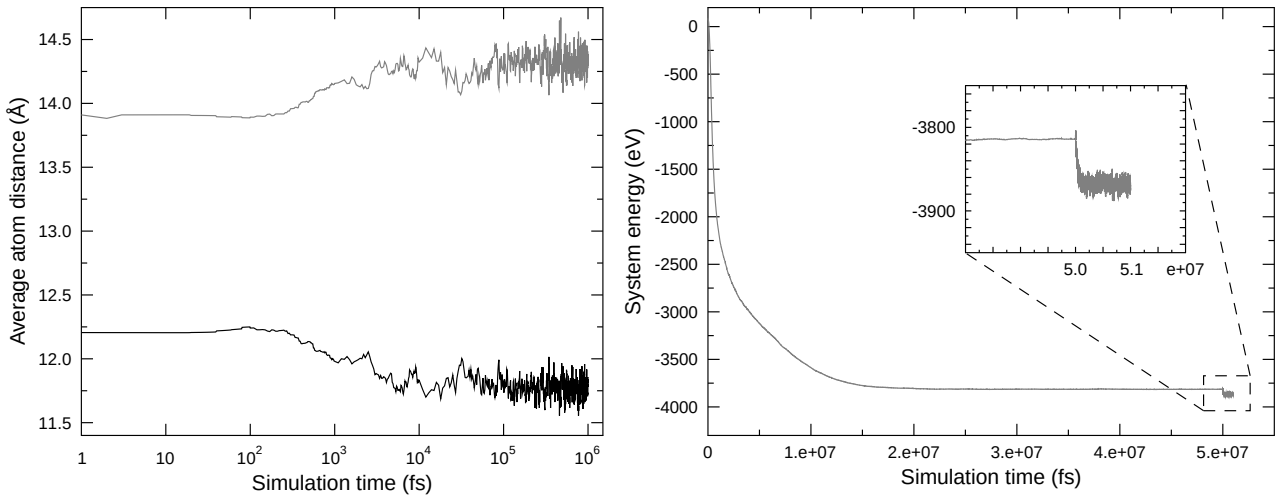

Figure 19: (a) The average atom distance from the center of mass of the cluster for Si (black) and Ge (grey) as a function of simulation time for a cluster of $Si_{0.5}Ge_{0.5}$ condensed using the Tersoff potential and further simulated using the SGCMC algorithm. (b) The total energy of this cluster as a function of simulation time during condensation (up to 50 ns) and the ensuing SGCMC run (inset graph). From publication **II**.

6.3 Publication III: Single layer deposition

While it would be possible to run deposition simulations using the clusters produced through MD condensation, actual experimental clusters are closer to the perfect form than any achieved computationally. Therefore, for the next two publications, clusters of pure Si and Ge used in deposition are made from scratch in an effort to make them better resemble their experimental counterparts. Such a cluster can be built by delimiting a spherical region within a larger sample of crystalline bulk and discarding all atoms not within it. A touch of realism is added by repeated annealing below the melting point in a process called *thermalizing*, which brings the cluster closer to the thermal equilibrium dictated by the potential used in the simulations. This process slightly reduces the sphericity and crystallinity of the cluster, which are perfect prior to thermalization.

In addition to thermalizing the deposition cluster, the bulk substrate also has to be thermalized in the same fashion. When this treatment is done before any deposition takes place, the surface reaches a more stable posture, characterized by asymmetric surface dimerization [89; 90; 91]. After this so-called *relaxation*, there are no excess stress factors in the interface between the deposited clusters and the substrate, signifying a more realistic system.

The concept of relaxation is also important during the consecutive deposition of multiple clusters. Just as when deposited on a bare substrate, clusters deposited on other clusters require the nascent interface to be completely relaxed. This defines an assumption made in the deposition simulations: once the system is thoroughly relaxed, it will not incur any significant changes until the next cluster is deposited, whether that happens in a matter of picoseconds or of milliseconds. Thus, even though the deposition of a single cluster is made to last a time Δt that is bearable in CPU time, and consecutive clusters are then deposited at the rate of $1/\Delta t$, this extremely rapid deposition rate should result in exactly the same layer as when deposited at a rate that is orders of magnitude slower, as in experimental work — barring macroscopic time-scale effects such as diffusion. For this work, Δt was determined as the time required for the system energy to stabilize to a constant value, which turned out to be one nanosecond.

When depositing clusters, the deposition energy is a crucial parameter. As was pointed out in Sect. 6.1, if two atomic bodies encountering each other have sufficient energy, they will coalesce and lose some information about their previous arrangement. Simulations have indeed shown how increasing the deposition energy results in increasing deformation of the deposited

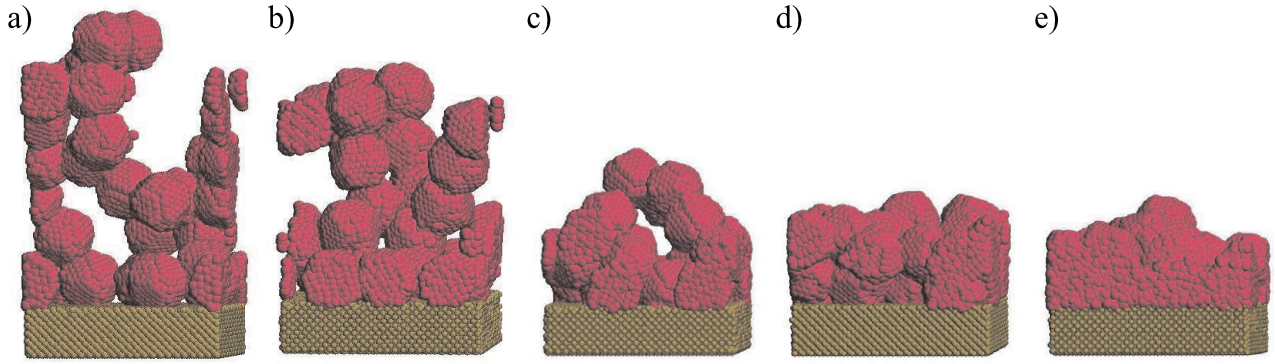

Figure 20: The visualization of deposited layers of 25 clusters with a deposition energy of a) 10 meV, b) 100 meV, c) 300 meV, d) 500 meV, and e) 1 eV. From publication **III**.

clusters [92; 93]. Thermal energy U and temperature T are linked by the equation

$$U = \frac{3}{2} N k_B T, \tag{30}$$

where N is the number of particles in a system [94]. For comparison, room temperature corresponds to a deposition energy U/N of nearly 40 meV/atom while the extreme annealing temperature of 6000 K corresponds to an energy of almost 0.8 eV/atom. With this in mind, deposition energies of 10 meV, 100 meV, 300 meV, 500 meV, and 1 eV per atom are chosen for this study. It should be noted that the first of these is lower than the thermal energy of the cluster at room temperature, which means that its effect when the cluster collides with the substrate is less than that of the random thermal movement of the individual atoms.

Some of the resulting layers are shown in Fig. 20, where the deformation of the clusters deposited with higher energies is clear. At thermal energies (below the aforementioned ∼40 meV/atom), the clusters simply touch upon the surface and stick to it due to the attractive interatomic forces at play. When stacking spherical objects, it is intuitively clear that there will be empty space left between them; in this case, this empty space forms the pores of the layer. As the deposition energy is increased, the amount of inter-cluster space decreases along with the porosity of the layer, until the layer becomes as dense as bulk, which happens with deposition energies somewhere around 1 eV/atom.

The porosity of a layer deposited using thermal energies is obviously the maximum porosity attainable using cluster deposition. This value has been experimentally determined to be just over 70% [95]; this fact is reinforced by the results for the 10 meV/atom depositions, which place the value somewhere between $P_{min} = 70\%$ and $P_{max} = 80\%$, as can be seen on the left side of Fig. 21. The difference between minimum and maximum porosity increases with

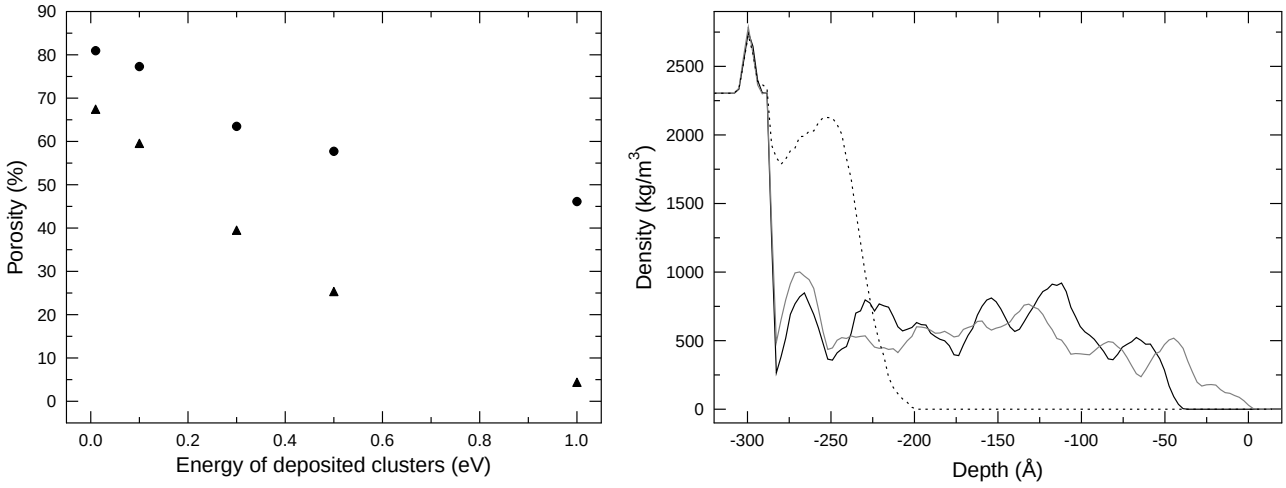

Figure 21: Left: the layer porosities P_{max} (circle) and P_{min} (triangle) as a function of deposition energy for runs of 30 Ge clusters deposited on a Si substrate. From publication **III**. Right: the density profiles of the layers deposited at 10 meV (black solid line), 100 meV (grey solid line), and 1 eV (black dashed line) per atom. The peak at the top of the bulk is due to surface dimerization.

deposition energy because the same number of clusters is deposited in each case, resulting in an ever thinner layer where variations in surface height have a proportionally larger impact. This is why it can be considered more descriptive at this size scale to map the distribution of void in a layer using a density profile such as the one on the right side of Fig. 21.

As a quantity, porosity still does have its uses. The discrepancy between P_{min} and P_{max} can be eliminated by growing a layer with a thickness much greater than the diameter of a single cluster, which can be done on a realistic time scale only experimentally. With an established dependence of deposition energy on the layer's porosity, the latter can be controlled to produce layers that, for example, weigh P% less than an ordinary layer or can store up to P% of the layer volume of another substance, the usefulness of which will be demonstrated below.

6.4 Publication IV: Multilayer formation

Single layers are deposited onto a crystalline substrate simulated with periodic boundary conditions that mimic the effects of bulk, *i.e.* the energy of deposition is absorbed by the substrate and diluted by the quasi-infinite amount of atoms. Clusters deposited on top of other clusters convey this energy in accordance with its magnitude: thermal energies have no effect, but higher energies are absorbed quickly enough to disrupt the structures of the colliding clusters. While this has a destructive effect on the topmost clusters of a layer, rapid absorption also means that

the reach of the disruption is not very long. In fact, even a casual glance at a deposited layer such as in Fig. 3 shows that the majority of the volume of the clusters remains undisturbed, and that the damage is limited to the cluster surfaces.

This brings up an interesting question: what happens if the deposition energy is changed *during* deposition? Going from high to low energy should pose no problems, since low-energy deposition can be done on a rough surface just as well as on a pristine substrate. But if the energy is increased, the question becomes whether or not a porous surface can support high-energy deposition as well as a substrate. It has been shown that the high-energy (several to tens of keV) heavy-ion irradiation of cluster-deposited layers disrupts the structure of the clusters and densifies the layer beyond any semblance of porosity [96]. Although when depositing a cluster of about 1000 atoms, the total cluster energy is in that same range, the individual atomic energy of 1 eV would by itself not suffice to cause that kind of damage. In addition, the atoms of an impinging cluster are bound together in a way that prevents the penetration of single atoms past the surface.

This gives the motivation to study the further high-energy deposition of clusters on top of previously deposited porous layers in an attempt to form porous multilayers. If the energy-induced disruption is indeed limited to within a few atoms of the collision interface, then there is no reason to believe that the porous assembly of thermally deposited clusters would collapse when bombarded with high-energy clusters. Instead, the porosity of the layer could be reduced if the high kinetic energy helps the deposited clusters enter the surface pores. Fortunately, due to the random locations of the deposited clusters, the depth of pores open to the surface is never large enough to be a concern in layers having practical thicknesses.

A sample deposition such as that shown in Fig. 22 proves that the impact of high-energy clusters indeed has a minimal effect on the structure of the porous layer onto which they are deposited. The density of the original layer stays relatively untouched until a certain point, above which the high-energy clusters can penetrate the surface pores. The depth of this penetration region is as small as 10 nm, along which the new layer eventually reaches bulk density. This means that the original porous layer becomes hidden beneath a new layer that can effectively function as a new substrate for further deposition. The enclosed porous layer(s) can then have a variety of practical uses: in addition to the aforementioned waveguiding and other optical apparatuses, the void-ridden layer can function as a storage compartment for materials that don't react with the layer element, *e.g.* hydrogen.

Because of the penetration, the multilayer structure becomes more complicated if the type of atom is changed along with the deposition energy. The 10-nm penetration region becomes a

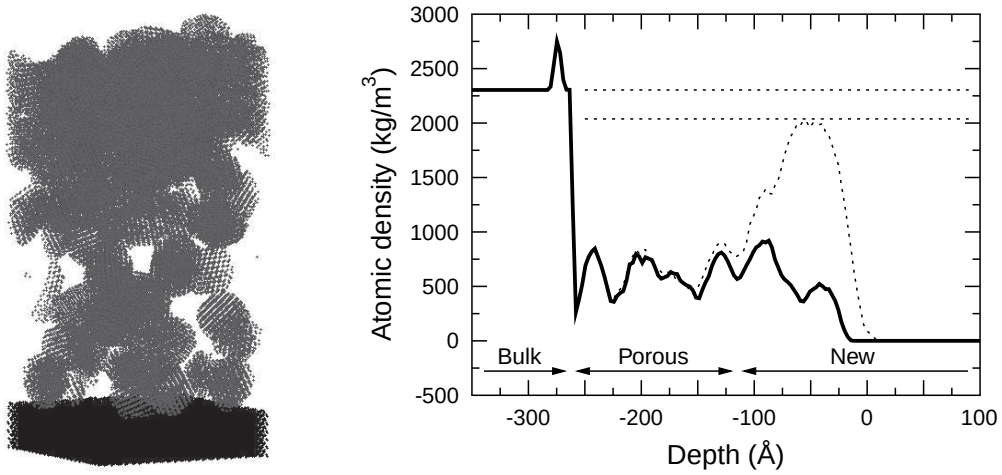

Figure 22: Left: a multilayer consisting of 90 germanium clusters of 1018 atoms (grey) on bulk silicon (black). The bottom 50 clusters form a porous layer, while the topmost 40 clusters are compressed to near bulk density. From publication **IV**. Right: the depth profile of the multilayer on the left. The solid black curve shows the profile of the original porous layer. The horizontal dotted lines show the bulk densities for silicon (higher) and germanium (lower). The dotted curve shows the total density of the multilayer.

mixture of clusters of the two elements, acquiring special optical and electronic characteristics. However, the relative significance of this effect is diminished if the deposited layers are much thicker than 10 nm. Furthermore, the penetration region thickness can be reduced if the high-energy clusters are deposited at an angle, although this requires raising the deposition energy to achieve the same low porosity.

The difference between clusters of different elements is clearly visible in simulated TEM imaging of the layers. As explained in Sect. 4.3, the beam electrons that survive through the entire sample incur a phase shift that differs according to what kind of electronic structure they encounter. This structure is obviously different for different elements, but in monoelemental systems, it can be affected by any deviation from crystalline bulk, such as porosity (or inversely, density). These effects are clear in Fig. 23, where some of the TEM images relevant to publications **III** and **IV** are presented.

In these images, the contrast is dominated by the dimer-bulk coupling seen at the bottom of each image. The contrast is set by matching white with the highest amplitude and black with the lowest, which in this case means the dimer monolayer and the crystalline bulk. Since the imaging software supplies its user with only these extreme values, it is therefore not possible to quantitatively analyze contrast differences in the deposited layers themselves. Instead, qualitative observations can be made: the higher density of a non-porous layer (a) as opposed to a

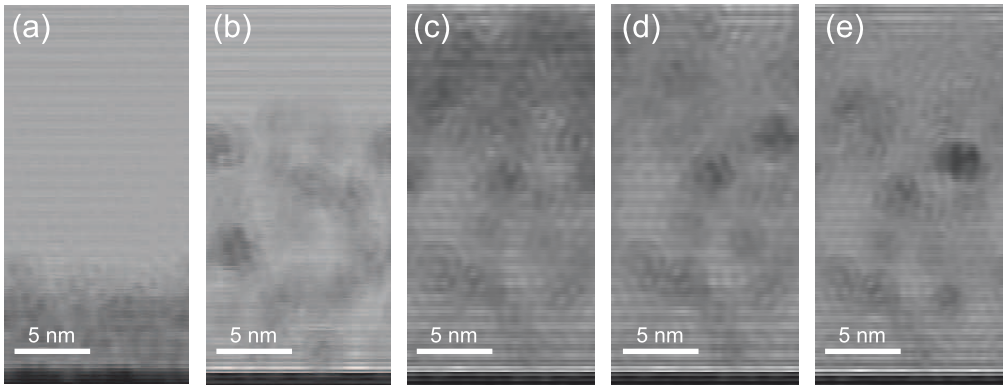

Figure 23: Simulated cross-sectional TEM images of Ge cluster layers deposited using an energy of (a) 1 eV/atom and (b) 10 meV/atom. On top of the latter, further depositions of (c) Ge clusters, (d) Si clusters, and (e) Si clusters deposited at an angle of 45°. The contrast between the two sets of images is not comparable. Images (a) and (b) from publication **III** and images (c) through (e) from publication **IV**.

porous layer (b) makes the non-porous image darker; the same effect can be seen in Si layers with a minute density difference (d and e); and yet, a layer of Ge (c) is darker than a layer of Si (d) that has a higher density.

The lack of consistent crystallinity in the new layers is also apparent in the images. At the top of the image in Fig. 23(d), there is a layer of Si with the same density as that of the crystalline substrate at the bottom of the image. Yet, the deposited layer has much lighter contrast than the bulk layer, indicating that there is a substantial phase difference in the electron beams traveling through each layer. Since the densities of the layers are almost the same, the lighter contrast can only be caused by having to pass through multiple grain boundaries during the voyage through the sample.

7 SUMMARY

It has been shown in this thesis that silicon and germanium atoms in vaporous form tend to condense into spherical or near-spherical clusters in an argon atmosphere, but that on occasion, the condensation results in imperfect clusters usually in the form of several spherical agglomerates sticking together. It is intuitively clear that two liquid droplets quickly form a single sphere when connected, but two solid droplets do not, which would suggest that the smaller agglomerates needed to be in a molten state to coalesce. However, knowledge of the failings of the interatomic potentials used in these simulations reveals that none of the clusters wholly melted at any time during condensation; instead, local melting could have been induced by the energy released by the collision of the agglomerates, which becomes increasingly unlikely as the size of the agglomerates increases. This suggests that there might be an upper limit to the size of the clusters that can be condensed into a spherical form.

Annealing these malformed clusters at the maximum temperature reached during the condensation simulations is a simple way to address the issue. However, the local temperature at the interface of two colliding agglomerates may well exceed the average value given for the whole system. Indeed, it is only as the annealing temperature is raised to extreme levels that the clusters become just about as spherical as most of the freshly condensed ones; in addition, their crystallinity is improved close to that of a perfect bulk crystal. The segregation of Ge atoms to the cluster surface, an effect already apparent in the condensation simulations, is not affected by annealing but is further strengthened with the additional use of a semi-grand-canonical Monte Carlo algorithm.

Whatever their method of formation, the benefits of Si and Ge clusters are best exploited in deposited films where the original morphologies of the clusters remain intact. This can be achieved by depositing the clusters at an energy low enough not to cause them decisive structural damage. Even below this limit, there is a range of energies that directly dictates the porosity of the layer; it is thus possible to grow a single layer with the desired porosity. A superposition of layers of differing porosities then results in a multilayer structure that could potentially function as *e.g.* a waveguide or a hydrogen storage container.

While porous multilayers have already been constructed using anodization, this method limits the end result to whatever can be carved out of bulk. The same kind of structure can be accomplished from a bottom-up perspective using cluster beam deposition; moreover, this other method does not suffer from the aforementioned limitation. Instead, to further tailor the optical and electronic properties of the multilayers, they can be made using clusters of more than

one element, whether they are arranged as alternating monoelemental layers, or single layers comprising nanocrystalline regions of more than one element. In a world where every path must be trod in the search for unforeseen technological advances, these new structures will surely find their place.

ACKNOWLEDGEMENTS

I wish to thank the head of the Department of Physics at the University of Helsinki, Professor Juhani Keinonen, and the head of the Division of Materials Physics, Professor Jyrki Räisänen, for providing the facilities for my PhD studies.

I am deeply indebted to Professor Kai Nordlund for supervising my thesis work. Thanks to his encouragement and support, I was able to start working in the field of atomistic simulations; and without his guidance, I could never have completed this work. He is truly an inspiration to any aspiring scientist.

I am especially grateful to two of my colleagues, Jani Kotakoski and Antti Tolvanen, for taking the time to advise me during the writing of this thesis. I am also thankful for the support of my other labmates, who made my working environment so enjoyable. A special thank-you goes out to my friend Eero Holmström for sharing in three of my favorite pastimes: music, philosophy, and beer.

I owe a debt of gratitude to my family for all the support they have given me over the years. My father Hannu, for showing me the way; my mother Sini, for always being there; and my brother Jouni, for showing me that I'm not alone. I am also grateful to my wife Enni for making these last efforts tolerable; and to our unborn son for making them necessary.

Finally, I wish to thank my friends, including but not limited to the members of the SOL Mixed Choir and the YL Male Voice Choir, for providing a valuable distraction during the years of my graduate studies.

Ari Harjunmaa

References

1. J. Chelikowski, in *Silicon: evolution and future of a technology*, edited by P. Siffert and E. F. Krimmel (Springer, Berlin, 2004), p. 1.

2. G. E. Moore, *Cramming more components onto integrated circuits*, Electronics **38**, 114 (1965).

3. R. R. King, A. Boca, W. Hong, X.-Q. Liu, D. Bhusari, D. Larrabee, K. M. Edmonson, D. C. Law, C. M. Fetzer, S. Mesropian, and N. H. Karam, in *Proceedings of 24th European photovoltaic solar energy conference* (Hamburg, Germany, 2009), pp. 55–61.

4. A. W. Bett, F. Dimroth, W. Guter, R. Hoheisel, E. Oliva, S. P. Philipps, J. Schöne, G. Siefer, M. Steiner, A. Wekkeli, E. Welser, M. Meusel, W. Köstler, and G. Strobl, in *Proceedings of 24th European photovoltaic solar energy conference* (Hamburg, Germany, 2009), pp. 1–6.

5. W. Guter, M. Meusel, W. Köstler, R. Kern, G. Siefer, R. Kellenbenz, and F. Dimroth, in *Proceedings of the international conference on concentrating photovoltaic systems* (Freiburg, Germany, 2010), pp. 3–6.

6. L. T. Canham, *Silicon quantum wire array fabrication by electrochemical and chemical dissolution of wafers*, Appl. Phys. Lett. **57**, 1046 (1990).

7. V. Lehmann and U. Gösele, *Porous silicon formation: A quantum wire effect*, Appl. Phys. Lett. **58**, 856 (1991).

8. P. M. Fauchet and J. von Behren, *The Strong Visible Luminescence in Porous Silicon: Quantum Confinement, not Oxide-Related Defects*, Phys. Stat. Sol. B **204**, R7 (1997).

9. R. Venkatasubramanian, D. P. Malta, M. L. Timmons, and J. A. Hutchby, *Visible light emission from quantized planar Ge structures*, Appl. Phys. Lett. **59**, 1603 (1991).

10. S. Gardelis, J. S. Rimmer, P. Dawson, B. Hamilton, R. A. Kubiak, T. E. Whall, and E. H. C. Parker, *Evidence for quantum confinement in the photoluminescence of porous Si and SiGe*, Appl. Phys. Lett. **59**, 2118 (1991).

11. M. Grätzel, *Photoelectrochemical cells*, Nature **414**, 338 (2001).

12. R. J. Archer, *Stain Films on Silicon*, J. Phys. Chem. Sol. **14**, 104 (1960).

13. T. Takagi, I. Yamada, and H. Takaoka, *Film formation technique by ionized-cluster beam*, Surf. Sci. **106**, 544 (1981).

14. G. Fuchs, M. Treilleux, F. S. Aires, B. Cabaud, P. Mélinon, and A. Hoareau, *Cluster-beam deposition for high-quality thin-films*, Phys. Rev. A **40**, 6128 (1989).

15. F. S. Aires, M. Treilleux, G. Fuchs, A. Hoareau, P. Mélinon, and B. Cabaud, *Size distribution of Bi clusters deposits on amorphous carbon substrates*, Z. Phys. D **12**, 149 (1989).

16. P. Mélinon, G. Fuchs, B. Cabaud, A. Hoareau, P. Jensen, V. Paillard, and M. Treilleux, *Low-energy cluster beam deposition — do you need it?*, J. de Phys. I **3**, 1585 (1993).

17. P. Mélinon, P. Kéghélian, B. Prével, A. Perez, G. Guiraud, and J. LeBrusq, *Nanostructured silicon films obtained by neutral cluster depositions*, J. Chem. Phys. **107**, 10278 (1997).

18. P. Mélinon, P. Kéghélian, B. Prével, V. Dupuis, A. Perez, B. Champagnon, Y. Guyot, M. Pellarin, J. Lermé, M. Broyer, J. L. Rousset, and P. Delichère, *Structural, vibrational, and optical properties of silicon cluster assembled films*, J. Chem. Phys. **108**, 4607 (1998).

19. I. Kwon, R. Biswas, G. S. Grest, and C. M. Soukoulis, *Molecular-dynamics simulation of amorphous and epitaxial Si film growth on Si(111)*, Phys. Rev. B **41**, 3678 (1990).

20. H. Haberland, Z. Insepov, and M. Moseler, *Molecular-dynamics simulation of thin-film growth by energetic cluster impact*, Phys. Rev. B **51**, 11061 (1995).

21. R. P. Feynman, *There's Plenty of Room at the Bottom.* A transcript of the talk is available online at http://www.zyvex.com/nanotech/feynman.html. A published version appears in Caltech's Engineering and Science February 1960 issue.

22. P. Buffat and J.-P. Borel, *Size effect on the melting temperature of gold particles*, Phys. Rev. A **13**, 2287 (1976), and references therein.

23. L. de Broglie, *Recherches sur la théorie des quanta*, Ph.D. thesis, Paris, 1924.

24. J. R. Hook and H. E. Hall, *Solid State Physics*, 2nd ed. (John Wiley & Sons, Chichester, 1991).

25. J. Singleton, *Band Theory and Electronic Properties of Solids* (Oxford University Press, New York, 2001).

26. M. Bawendi, M. L. Steigerwald, and L. E. Brus, *The quantum mechanics of larger semiconductor clusters ("quantum dots")*, Annu. Rev. Phys. Chem. **41**, 477 (1990).

27. O. Björneholm, G. Öhrwall, and M. Tchaplyguine, *Free clusters studied by core-level spectroscopies*, Nucl. Instr. and Meth. A **601**, 161 (2009), and references therein.

28. J. R. Chelikowsky, *Transition from Metallic to Covalent Structures in Silicon Clusters*, Phys. Rev. Lett **60**, 2669 (1988).

29. P. Mélinon, V. Paillard, V. Dupuis, A. Perez, P. Jensen, A. Hoareau, J. P. Perez, J. Tuaillon, M. Broyer, J. L. Vialle, M. Pellarin, B. Baguenard, and J. Lermé, *From free clusters to cluster-assembled materials*, Int. J. Mod. Phys. B **9**, 339 (1995).

30. R. Sayle and E. J. Milner-White, *RasMol: Biomolecular graphics for all*, Trends in Bioch. Sci. **20**, 374 (1995).

31. K. Kordás, A. E. Pap, S. Beke, and S. Leppävuori, *Optical properties of porous silicon. Part I: Fabrication and investigation of single layers*, Opt. Mat. **25**, 251 (2004).

32. M. A. Laguna, V. Paillard, B. Kohn, M. Ehbrecht, F. Huisken, G. Ledoux, R. Papoular, and H. Hofmeister, *Optical properties of nanocrystalline silicon thin films produced by size-selected cluster beam deposition*, J. Lum. **80**, 223 (1999).

33. G. Vincent, *Optical properties of porous silicon superlattices*, Appl. Phys. Lett. **64**, 2367 (1994).

34. M. G. Berger, C. Dieker, M. Thönissen, L. Vescan, H. Lüth, H. Münder, W. Theiß, M. Wernke, and P. Grosse, *Porosity superlattices: a new class of Si heterostructures*, J. Phys. D: Appl. Phys. **27**, 1333 (1994).

35. M. G. Berger, M. Thönissen, R. Arens-Fischer, H. Münder, H. Lüth, M. Arntzen, and W. Theiß, *Investigation and design of optical properties of porosity superlattices*, Thin Solid Films **255**, 313 (1995).

36. V. P. Bondarenko, A. M. Dorofeev, and N. M. Kazuchits, *Optical waveguide based on oxidized porous silicon*, Micr. Eng. **28**, 447 (1995).

37. A. Loni, L. T. Canham, M. G. Berger, R. Arens-Fischer, H. Münder, H. Lüth, H. F. Arrand, and T. M. Benson, *Porous silicon multilayer optical waveguides*, Thin Solid Films **276**, 143 (1996).

38. B. J. Alder and T. E. Wainwright, *Phase Transition for a Hard Sphere System*, J. Chem. Phys. **27**, 1208 (1957).

39. B. J. Alder and T. E. Wainwright, *Studies in Molecular Dynamics. I. General Method*, J. Chem. Phys. **31**, 459 (1959).

40. B. J. Alder and T. E. Wainwright, *Studies in Molecular Dynamics. II. Behavior of a Small Number of Elastic Spheres*, J. Chem. Phys. **33**, 1439 (1960).

41. K. Nordlund, M. Ghaly, R. Averback, M. Caturla, T. D. de la Rubia, and J. Tarus, *Defect production in collision cascades in elemental semiconductors and fcc metals*, Phys. Rev. B **57**, 7556 (1998).

42. M. Ghaly, K. Nordlund, and R. Averback, *Molecular dynamics investigations of surface damage produced by kiloelectronvolt self-bombardment of solids*, Phil. Mag. A **79**, 795 (1999).

43. S. Plimpton, *Fast Parallel Algorithms for Short-Range Molecular Dynamics*, J. Comp. Phys. **117**, 1 (1995), software available at http://lammps.sandia.gov/.

44. K. Nordlund, *Molecular dynamics simulation of ion ranges in the 1–100 keV energy range*, Comp. Mat. Sci. **3**, 448 (1995).

45. M. Born and R. Oppenheimer, *Zur Quantentheorie der Molekeln*, Ann. Phys. **359**, 457 (1927).

46. A. Caro and M. Victoria, *Ion-electron interaction in molecular-dynamics cascades*, Phys. Rev. A **40**, 2287 (1989).

47. M. W. Finnis, P. Agnew, and A. J. E. Foreman, *Thermal excitation of electrons in energetic displacement cascades*, Phys. Rev. B **44**, 567 (1991).

48. J. E. Lennard-Jones, *On the Determination of Molecular Fields. I. From the Variation of the Viscosity of a Gas with Temperature*, Proc. Roy. Soc. Lond. A **106**, 441 (1924).

49. J. E. Lennard-Jones, *On the Determination of Molecular Fields. II. From the Equation of State of a Gas*, Proc. Roy. Soc. Lond. A **106**, 463 (1924).

50. J. A. White, *Lennard-Jones as a model for argon and test of extended renormalization group calculations*, J. Chem. Phys. **111**, 9352 (1999).

51. F. H. Stillinger and T. A. Weber, *Computer simulation of local order in condensed phases of silicon*, Phys. Rev. B **31**, 5262 (1985).

52. J. Tersoff, *Modeling solid-state chemistry: Interatomic potentials for multicomponent systems*, Phys. Rev. B **39**, 5566 (1989).

53. D. P. Landau and K. Binder, *A guide to Monte Carlo simulations in statistical physics*, 2nd ed. (Cambridge University Press, New York, 2005).

54. P. A. Stadelmann, *EMS – a software package for electron diffraction analysis and HREM image simulation in materials science*, Ultramicroscopy **21**, 131 (1987).

55. M. Knoll and E. Ruska, *Das Elektronenmikroskop*, Z. Physik **78**, 318 (1932).

56. M. Knoll and E. Ruska, *Beitrag zur geometrischen Elektronenoptik. I*, Ann. Physik **404**, 607 (1932).

57. E. Ruska, *Über Fortschritte im Bau und in der Leistung des magnetischen Elektronenmikroskops*, Z. Physik **87**, 580 (1934).

58. E. Ruska, *Über ein magnetisches Objektiv für das Elektronenmikroskop*, Z. Physik **89**, 90 (1934).

59. M. de Graef, *Introduction to Conventional Transmission Electron Microscopy* (Cambridge University Press, Cambridge, 2003).

60. E. J. Kirkland, *Advanced Computing in Electron Microscopy* (Plenum Press, New York, 1998).

61. J. M. Cowley and A. F. Moodie, *The scattering of electrons by atoms and crystals. I. A new theoretical approach*, Acta Cryst. **10**, 609 (1957).

62. P. Goodman and A. F. Moodie, *Numerical evaluation of N-beam wave functions in electron scattering by the multislice method*, Acta Cryst. A **30**, 280 (1974).

63. J. G. Allpress, E. A. Hewat, A. F. Moodie, and J. V. Sanders, *n-Beam lattices images. I. Experimental and computed images of* $W_4Nb_{26}O_{77}$, Acta Cryst. A **28**, 528 (1972).

64. J. G. Allpress and J. V. Sanders, *The direct observation of the structure of real crystals by lattice imaging*, J. Appl. Cryst. **6**, 165 (1973).

65. C. Hetherington, *Aberration correction for TEM*, Materials Today **7**, 50 (2004), and references therein.

66. L. Boltzmann, *Vorlesungen über Gastheorie — I. Theil* (Verlag von J. A. Barth, Leipzig, 1896).

67. L. Boltzmann, *Vorlesungen über Gastheorie — II. Theil* (Verlag von J. A. Barth, Leipzig, 1898).

68. E. T. Jaynes, *Gibbs vs Boltzmann entropies*, Amer. J. of Phys. **33**, 391 (1965).

69. H. J. C. Berendsen, J. P. M. Postma, W. F. van Gunsteren, A. DiNola, and J. R. Haak, *Molecular dynamics with coupling to an external bath*, J. Chem. Phys. **81**, 3684 (1984).

70. E. E. Zhurkin and M. Hou, *Structural and thermodynamic properties of elemental and bimetallic nanoclusters: an atomic scale study*, J. Phys.: Condens. Matter **12**, 6735 (2000).

71. W. D. Knight, K. Clemenger, W. A. de Heer, W. A. Saunders, M. Y. Chou, and M. L. Cohen, *Electronic Shell Structure and Abundances of Sodium Clusters*, Phys. Rev. Lett. **52**, 2141 (1984).

72. M. Moseler, B. Huber, H. Häkkinen, U. Landman, G. Wrigge, M. A. Hoffmann, and B. v. Issendorff, *Thermal effects in the photoelectron spectra of Na_N^- clusters ($N = 4 - 19$)*, Phys. Rev. B **68**, 165413 (2003).

73. T. P. Martin, *Shells of atoms*, Phys. Rep. **273**, 199 (1996).

74. H. Wadell, *Volume, Shape, and Roundness of Quartz Particles*, J. Geol. **43**, 250 (1935).

75. K. Nordlund and R. S. Averback, *Point defect movement and annealing in collision cascades*, Phys. Rev. B **56**, 2421 (1997).

76. J. L. Morán-López and L. M. Falicov, *Segregation and short-range order properties at the boundaries of two-dimensional bimetallic clusters*, Surf. Sci. **79**, 109 (1979).

77. J. L. Rousset, B. C. Khanra, A. M. Cadrot, F. J. C. S. Aires, A. J. Renouprez, and M. Pellarin, *Investigations on supported bimetallic PdPt nanostructures*, Surf. Sci. **352–354**, 583 (1996).

78. J. Tarus, M. Tantarinmäki, and K. Nordlund, *Segregation in SiGe clusters*, Nucl. Instr. and Meth. B **228**, 51 (2005).

79. R. J. Jaccodine, *Surface Energy of Germanium and Silicon*, J. Electrochem. Soc. **110**, 524 (1963).

80. F. Voigt, R. Brüggemann, T. Unold, F. Huisken, and G. H. Bauer, *Porous thin films grown from size-selected silicon nanocrystals*, Mater. Sci. and Eng. C **25**, 584 (2005).

81. C. G. Granqvist and R. A. Buhrman, *Ultrafine metal particles*, J. Appl. Phys. **47**, 2200 (1976).

82. R. A. Buhrman and C. G. Granqvist, *Log-normal size distributions from magnetization measurements on small superconducting Al particles*, J. Appl. Phys. **47**, 2220 (1976).

83. T. G. Dietz, M. A. Duncan, D. E. Powers, and R. E. Smalley, *Laser production of supersonic metal cluster beams*, J. Chem. Phys. **74**, 6511 (1981).

84. H. Haberland, M. Karrais, and M. Mall, *A new type of cluster and cluster ion source*, Z. Phys. D **20**, 413 (1991).

85. K. Meinander, *Growth and Modification of Cluster-Assembled Thin Films*, Ph.D. thesis, Helsinki, 2009.

86. M. Forsblom and G. Grimvall, *How superheated crystals melt*, Nature Mater. **4**, 388 (2005).

87. M. Forsblom and G. Grimvall, *Homogeneous melting of superheated crystals: Molecular dynamics simulations*, Phys. Rev. B **72**, 054107 (2005).

88. J. Nord, *Modeling of high-dose radiation damage in semiconductors*, Ph.D. thesis, Helsinki, 2003.

89. R. E. Schlier and H. E. Farnsworth, *Structure and Adsorption Characteristics of Clean Surfaces of Germanium and Silicon*, J. Chem. Phys. **30**, 917 (1959).

90. D. J. Chadi, *Atomic and Electronic Structures of Reconstructed Si(100) Surfaces*, Phys. Rev. Lett. **43**, 43 (1979).

91. M. A. Bowen, J. D. Dow, and R. E. Allen, *Si(100) surface states: A success for the (2 × 1) asymmetric dimer model*, Phys. Rev. B **26**, 7083 (1982).

92. K. Meinander, K. Nordlund, and J. Keinonen, *Size dependent epitaxial cluster deposition: The effect of deposition energy*, Nucl. Instr. and Meth. B **242**, 161 (2006).

93. K. Meinander and K. Nordlund, *Modeling of film growth by cluster deposition: The effect of size and energy*, Phys. Rev. B **79**, 235435 (2009).

94. D. V. Schroeder, *An Introduction to Thermal Physics* (Addison-Wesley, Reading, MA, 1999).

95. D. Amans, S. Callard, A. Gagnaire, and J. Joseph, *Ellipsometric study of silicon nanocrystal optical constants*, J. Appl. Phys. **93**, 4173 (2003).

96. K. Meinander and K. Nordlund, *Irradiation-induced densification of cluster-assembled thin films*, Phys. Rev. B **79**, 045411 (2009).